Generalization of the Lambertian Model and Implications for Machine Vision

Michael Oren and Shree K. Nayar

CUCS-057-92

oren@cs.columbia.edu
nayar@cs.columbia.edu

Department of Computer Science
Columbia University
New York, N.Y. 10027

November, 1992

Revised: February, 1994

Minor revision: September, 1996

Contents

i

Abstract

Lambert's model for diffuse reflection is extensively used in computational vision. It is used explicitly by methods such as shape from shading and photometric stereo, and implicitly by methods such as binocular stereo and motion detection. For several real-world objects, the Lambertian model can prove to be a very inaccurate approximation to the diffuse component. While the brightness of a Lambertian surface is independent of viewing direction, the brightness of a rough diffuse surface increases as the viewer approaches the source direction. A comprehensive model is developed that predicts reflectance from rough diffuse surfaces. The model accounts for complex geometric and radiometric phenomena such as masking, shadowing, and interreflections between points on the surface. Experiments have been conducted on real samples, such as, plaster, clay, sand, and cloth. All these surfaces demonstrate significant deviation from Lambertian behavior. The reflectance measurements obtained are in strong agreement with the reflectance predicted by the proposed model. The paper is concluded with a discussion on the implications of these results for machine vision.

1 Introduction

One of the primary goals of a machine vision system is to recover physical properties of a scene from images. Image brightness values are closely related to the reflectance properties of points in the scene. Hence, accurate reflectance models are fundamental to the advancement of machine vision. Several mechanisms involved in the reflection process are reviewed in [Nayar *et al.*-1991b][Tagare and deFigueiredo-1991]. These mechanisms, or components, can be classified into two broad categories; diffuse and specular [1]. A surface that obeys Lambert's Law [Lambert-1760] appears equally bright from all viewing directions. This model for diffuse reflection was advanced by Lambert over 200 years ago and remains one of the most widely used models in machine vision. It is used explicitly by shape recovery techniques such as shape from shading and photometric stereo. It is also invoked by vision techniques such as binocular stereo and motion detection to solve the correspondence problem. In the field of remote sensing, the Lambertian model is often used to apply brightness corrections to images of the same scene obtained under different illumination conditions. The widespread use of the Lambertian model arises from its simplicity and because it does reasonably well in approximating reflection from a wide range of matte surfaces.

For several real-world objects, however, the Lambertian model can prove to be a poor and inadequate approximation to the diffuse component. Figure 1(a) shows a real image of a clay vase obtained using a CCD camera. The vase is illuminated by a single distant light source in the same direction as the sensor. Figure 1(b) shows a rendered image of a vase with the same shape as the one shown in Figure 1(a). This image is rendered using the Lambertian model, and the same illumination direction as in the case of the real vase. As expected, the Lambertian model predicts that the brightness of the cylindrical vase will decrease as we approach the occluding boundaries on both sides. However, the real vase is very flat in appearance, image brightness remaining almost constant over the entire surface. The vase is clearly *not* Lambertian in reflectance[2]. The deviation from Lambertian behavior illustrated above can be significant for a variety of other real-world materials, such as, concrete, sand, and cloth. An accurate model that describes diffuse reflectance from such common surfaces is needed for both qualitative analysis of images as well as accurate estimation of surface properties such as shape and reflectance.

---

[1] The specular components result from the reflection of incident light at the interface between two media, for instance, air and an object in the scene. This is a surface phenomenon. The diffuse component results from light rays that penetrate layers of the surface, undergo multiple reflections and refractions, and re-emerge at the surface. This mechanism is also referred to as body reflection. See [Nayar *et al.*-1991b, Tagare and deFigueiredo-1991] for details.

[2] Note that the real vase does not have any significant specular component, in which case, a vertical highlight would have appeared in the middle.
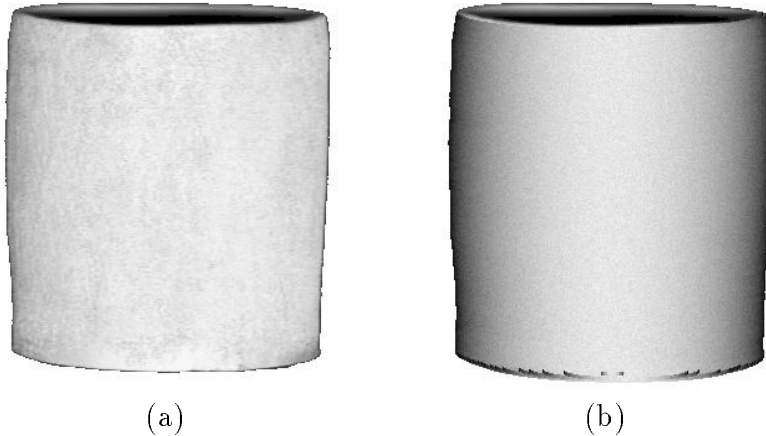
Figure 1: (a) Real image of a cylindrical clay vase. (b) Image of the vase rendered using the Lambertian reflectance model. In both cases, illumination is from the viewing direction.

What makes the vase shown in Figure 1(a) non-Lambertian? We will show that the primary cause for this deviation is surface roughness. In the areas of machine vision, remote sensing, and computer graphics, the magnification of the imaging system used can vary substantially from one scene to the next. Figure 2 illustrates the relationship between magnification and reflectance. The surface may be viewed as a collection of planar facets. At high magnification, each picture element (pixel) includes a single facet. At lower magnifications (used in the case of outdoor scenes), each pixel can include a large number of facets. Though the Lambertian assumption is often reasonable when looking at a single planar facet, the reflectance is not Lambertian when a collection of facets is imaged onto a single pixel. The deviation from Lambertian behavior is significant for very rough surfaces, and increases with the angle of incidence. In this paper, we develop a comprehensive model that predicts reflectance from rough diffuse surfaces, and provide experimental results that support the model. The Lambertian model is a special case, or instance, of the proposed model.

The topic of rough diffuse surfaces has been extensively studied in the areas of applied physics and geophysics. The following is a brief summary of previous results on the subject. In 1924, Opik [Öpik-1924] designed an empirical model to describe the non-Lambertian behavior of the moon. In 1941, Minnaert [Minnaert-1941] modified Opik's model to obtain the following reflectance function:

$$f_r = \frac{k+1}{2\pi}(\cos\theta_i \cos\theta_r)^{(k-1)} \qquad (0 \le k \le 1)$$

where, θ_i and θ_r are the polar angles of incidence and reflection, and k is a measure of surface roughness. This function was designed to obey Helmholtz's reciprocity principle (see [Beckmann and Spizzichino-1963]) but is not based on any theoretical foundation. It assumes that the radiance of non-Lambertian diffuse surfaces is symmetrical with respect to the surface normal, an assumption that proves to be incorrect. Hapke and van
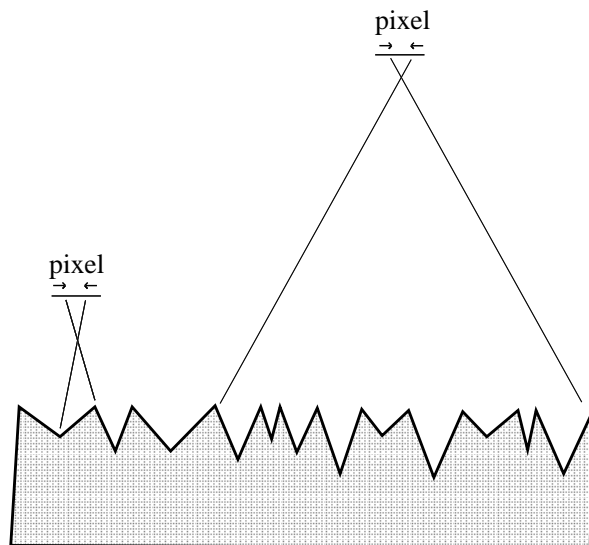
Figure 2: The roughness of a surface causes its reflectance properties to vary with image magnification.

Horn [Hapke and van Horn-1963] also obtained reflectance measurements from rough diffuse surfaces by varying the source direction for a fixed sensor direction. They found the peak of the radiance function to be shifted from the peak position expected for a Lambertian surface. This was interpreted as a minor discrepancy and the Lambertian model was assumed to be a reasonable approximation. Our measurements show that non-Lambertian behavior is clearly noticeable and significant when viewer direction is varied rather than source direction.

The above studies were attempts to design reflectance models based on measured reflectance data. In contrast, several investigators developed theoretical models for diffuse reflection from rough surfaces. These efforts were motivated primarily by the reflectance characteristics of the moon. Infrared emission and visible light reflection from the moon (see [Orlova-1956, Siegel and Howell-1972]) indicate that the moon's surface radiates more energy back in the direction of the source (the sun) than in the normal direction or in the forward direction. This phenomenon is referred to as *backscattering*[3]. Smith [Smith-1967] modeled the roughness of the moon as a random process and assumed each point on the surface to be Lambertian in reflectance. Smith's analysis, however,

---

[3]A different backscattering mechanism, called retroreflection or opposition effect, produces a sharp peak close to the source direction (see [Hapke and van Horn-1963, Kuga and Ishimaru-1984, Tsang and Ishimaru-1984, Oetking-1966]). This is not the mechanism discussed in this paper. A recent article by Hapke *et al.* [Hapke *et al.*-1993] throws new light on this mechanism. It is seldom encountered in machine vision since it is observed only when the sensor and source are within a few degrees from each other; a situation difficult to emulate in practice without the source or the sensor occluding the other.

was confined to the plane of incidence and is not easily extensible to reflections outside this plane. Further, Smith's model does not account for interreflection effects. Buhl et al. [Buhl *et al.*-1968] modeled the surface as a collection of spherical cavities. They analyzed interreflections using this surface geometry, but did not present a complete reflectance model that accounts for masking and shadowing effects for arbitrary angles of reflection and incidence. Subsequently, Hering and Smith [Hering and Smith-1970] derived a detailed thermal emission model for surfaces modeled as a collection of V-cavities. However, all the cavities are assumed to be identical and aligned in the same direction, namely, perpendicular to the source-viewer plane. This model is also limited to reflections in the plane of incidence.

Recently, in computer graphics, Poulin and Fournier [Poulin and Fournier-1990] derived a diffuse reflectance function for anistropic surfaces modeled as a collection of parallel cylindrical sections. This result however cannot be applied to surfaces with isotropic roughness. Other researchers in computer graphics have numerically pre-computed fairly complex reflectance functions and stored the results in the form of look-up tables (for examples, see [Cabral *et al.*-1987] [Kajiya-1991]). While rendering an image, parameters such as the angles of incidence and reflectance are used to index the table and read surface radiance values. This approach can be effective for graphics rendering but does not replace the need for accurate reflectance functions.

The model presented is this paper can be applied to isotropic as well as anisotropic rough surfaces, and can handle arbitrary source and viewer directions. Further, it takes into account complex geometrical effects such as masking, shadowing, and interreflections between points on the surface. We begin by modeling the surface as a collection of long symmetric V-cavities. Each V-cavity has two opposing facets and each facet is assumed to be much larger than the wavelength of incident light. This surface model was used by Torrance and Sparrow [Torrance and Sparrow-1967] to describe specular reflection from rough surfaces. Here, we assume the facets to be Lambertian in reflectance[4]. First, a reflectance model is developed for anisotropic surfaces with one type of V-cavities, and with all cavities aligned in the same direction on the surface plane. This result is then used to derive a model for the more general case of isotropic surfaces that have normal facet distributions with zero mean and arbitrary standard deviation (σ). The standard deviation parametrizes the macroscopic roughness of the surface. Figure 3 shows three images of spheres rendered using the proposed reflectance model. In all three cases, the sphere is illuminated from the viewer direction. In the first case, $\sigma = 0$, and hence the sphere is Lambertian in reflectance. As the roughness increases, the sphere begins to appear flatter. In the extreme roughness case shown in Figure 3(c), the sphere appears like a flat disc with nearly constant brightness. This phenomenon has been widely observed and reported in the case of the full moon.

---

[4]This assumption does not limit the implications of the reflectance model presented here. The non-Lambertian behavior reported here is expected for a wide range of local diffuse reflectance models (see [Chandrasekhar-1960], for example) since surface roughness is shown to play a dominant role.
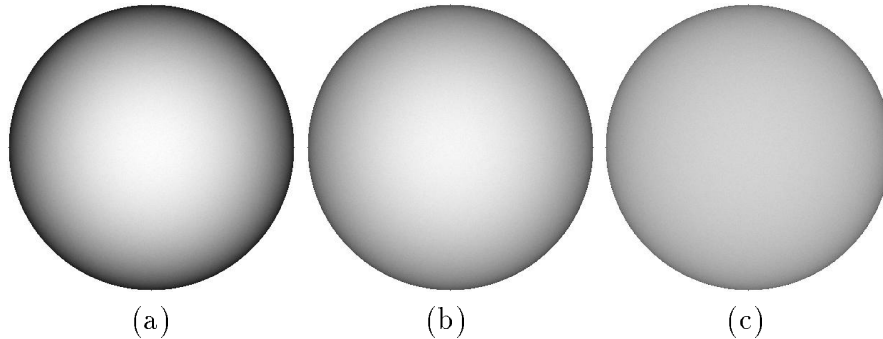
4

Figure 3: Images of spheres rendered using the proposed reflectance model: (a) $\sigma = 0$ (Lambertian sphere); (b) $\sigma = 20°$; (c) $\sigma = 40°$.

Several experimental results are presented to demonstrate the accuracy of the derived model. These experiments were conducted on commonplace samples such as sand, plaster, wood, and cloth. In all cases, reflectance predicted by the model was found to be in strong agreement with measurements. These results illustrate that the deviation from Lambertian behavior can be substantial. We conclude with a discussion on the implications of the proposed model for machine vision. First, we show that images of rough diffuse objects can be accurately described using the proposed model. Next, we study reflectance maps generated using the Lambertian model and the proposed model. As the roughness of the surface increases, the reflectance map varies from Lambertian to the linear reflectance map [Horn-1986] previously hypothesized for lunar reflectance. Finally, we demonstrate the application of the model to shape recovery using photometric stereo. While the new model accurately estimates the shape of a rough object, the Lambertian model produces large errors in surface orientation.

The results presented in this paper demonstrate two points that are fundamental to computer vision. (a) Several real-world objects have diffuse components that are significantly non-Lambertian. The reflectance of such objects cannot be accurately described using previous models. (b) The model presented in this paper can be used by vision algorithms to analyze images of diffuse surfaces and recover accurate shape information.

2   Radiometric Definitions

In this section, we define radiometric concepts that are used in the remaining of this paper. These concepts are discussed in detail in [Nicodemus *et al.*-1977]. Figure 4 shows a surface element dA illuminated from the direction $\hat{s} = (\theta_i, \phi_i)$ and viewed by a sensor in the direction $\hat{v} = (\theta_r, \phi_r)$, where θ and ϕ denote polar and azimuth angles, respectively. The sensor subtends an infinitesimal solid angle $d\omega_r$ from any point on the surface.

The light energy reflected by the surface patch is proportional to the light incident
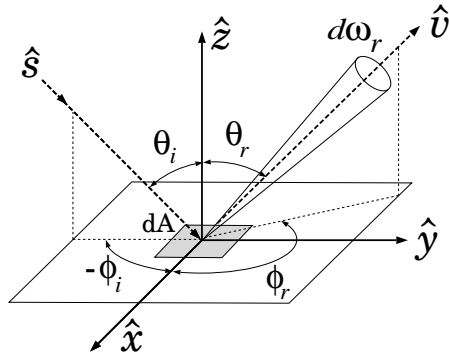
5

Figure 4: Geometry used to define radiometric terms.

on it. *Irradiance* is defined as the light flux incident per unit surface area:

$$E(\theta_i, \phi_i) = \frac{d\Phi_i(\theta_i, \phi_i)}{dA} \tag{1}$$

This is the directional irradiance of the surface as it represents light energy incident from the direction (θ_i, ϕ_i). The *total irradiance* of the surface is the flux incident from all directions and may be denoted simply as E. The brightness measured by the sensor is proportional to the *radiance* of the surface patch in the direction (θ_r, ϕ_r). Surface radiance is defined as:

$$L_r(\theta_r, \phi_r; \theta_i, \phi_i) = \frac{d\Phi_r(\theta_r, \phi_r; \theta_i, \phi_i)}{dA \, \cos\theta_r \, d\omega_r} \tag{2}$$

It is the flux radiated by the surface per unit solid angle, per unit *foreshortened* area. It depends on the direction of illumination and the sensor direction. The relationship between irradiance and radiance of a surface is determined by its reflectance properties. The *bi-directional reflectance distribution function (BRDF)* is defined as the ratio of radiance to irradiance:

$$f_r(\theta_r, \phi_r; \theta_i, \phi_i) = \frac{dL_r(\theta_r, \phi_r; \theta_i, \phi_i)}{dE(\theta_i, \phi_i)} \tag{3}$$

All the above definitions are general, in that, they are valid for surfaces with any reflectance characteristics. For an *isotropic* surface, radiance and *BRDF* do not change if the surface is rotated about its normal vector. For such surfaces, the *BRDF* is simply:

$$f_r(\theta_r, \theta_i, \phi_r - \phi_i) = \frac{dL_r(\theta_r, \theta_i, \phi_r - \phi_i)}{dE(\theta_i)} \tag{4}$$

A Lambertian surface is an ideal diffuser whose radiance is independent of the viewing direction of the sensor; it appears equally bright from all directions. Its *BRDF* is $f_r = \frac{\rho}{\pi}$ where the *albedo* ρ represents the fraction of incident energy that is reflected by the surface.

6

3   Surface Roughness Model

There are several ways of modeling surface roughness. The general approach is to select a model that is capable of representing real surfaces and at the same time easy to use during the mathematical development of the reflectance model. All surface models found in applied physics and geophysics literature can be divided into two broad categories. In the first case, the surface is modeled as a random process (see [Beckmann-1965, Wagner-1966, Smith-1967]). Using this approach, it is difficult to derive a reflectance model for arbitrary source and viewer directions, and to analyze interreflections. In the second category, surfaces are assumed to be composed of several elements with some primitive shape, for example, spherical cavities, V-cavities, holes, etc (see [Buhl *et al.*-1968, Torrance and Sparrow-1967]). As shown in this paper, the effects of shadowing, masking, and interreflection need to be analyzed in order to obtain an accurate reflectance model. To accomplish this, we use the roughness model proposed by Torrance and Sparrow [Torrance and Sparrow-1967] that assumes the surface to be composed of long symmetric V-cavities (see Figure 5). Each cavity consists of two planar facets. The width of each facet is assumed to be small compared to its length. The roughness of the surface is specified using a probability function for the distribution of facet slopes.
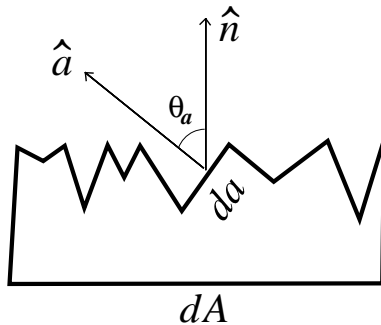

Figure 5: Surface modeled as a collection of V-cavities.

The V-cavity roughness model can be used to describe surfaces with both isotropic as well as anisotropic (directional) roughness. We assume each facet area da is small compared to the area dA of the surface patch that is imaged by a single sensor pixel. Hence, each pixel includes a very large number of facets. Further, the facet area is large compared to the wavelength λ of incident light and therefore geometrical optics can be used to derive the reflectance model. The above assumptions can be summarized as:

$$\lambda^2 \ll da \ll dA \tag{5}$$

The facets could be relatively small as in the case of sand and plaster, or large as in the case of outdoor scenes of terrain.

Slope-Area Probability Distribution:

We denote the slope and orientation of each facet in the V-cavity model as (θ_a, ϕ_a). Torrance and Sparrow have assumed all facets to have equal area da. They use the distribution $N(\theta_a, \phi_a)$ to represent the number of facets per unit surface area that have the normal $\hat{a} = (\theta_a, \phi_a)$. Here, we use a distribution function to represent the fraction of the surface area that is occupied by facets with a given normal. This is referred to as the *slope-area distribution* $P(\theta_a, \phi_a)$. The facet-number and slope-area distributions are related as follows:

$$P(\theta_a, \phi_a) = N(\theta_a, \phi_a)\, da\, \cos\theta_a \tag{6}$$

The slope-area distribution is easier to use than the facet-number distribution in the following model derivation. For isotropic surfaces, $N(\theta_a, \phi_a) = N(\theta_a)$ [5] and $P(\theta_a, \phi_a) = P(\theta_a)$, since the distributions are rotationally symmetric with respect to the global surface normal $\hat{n}$.

4 Reflectance Model

In this section, we derive a reflectance model for rough diffuse surfaces. The V-cavity model is used to describe surface geometry and each facet on the surface is assumed to be Lambertian in reflectance. The following three types of surfaces with different slope-area distributions are examined. (a) **Uni-directional Single-Slope Distribution**: This distribution results in a non-isotropic surface where all facets have the same slope and all cavities are aligned in the same direction. (b) **Isotropic Single-Slope Distribution**: Here, all facets have the same slope but they are uniformly distributed in orientation on the surface plane. (c) **Gaussian Distribution**: This is the most general case examined where the slope-area distribution is assumed to be normal with zero mean. The roughness of the surface is determined by the standard deviation of the normal distribution. The reflectance model obtained for each of the above surface types is used to derive the succeeding one.

Effect of Roughness on Diffuse Reflectance:

Before we proceed to derive reflectance models for the above-mentioned surface types, a brief illustration of the effect of roughness on diffuse reflection would be useful. Consider, for the purpose of discussion, the single V-cavity shown in Figure 6. Both facets of the cavity are fully illuminated by a distant source on the right side. If the facets are Lambertian with equal albedo, the left facet appears brighter than the right one as it receives more incident light. If the V-cavity is viewed from the left side by a distant observer, a larger fraction of the foreshortened cavity area is dark and a smaller fraction is bright. As the observer moves to the right, towards the source direction, the fraction of brighter area increases while that of the darker area decreases. Consequently,

---

[5] In [Torrance and Sparrow-1967], $N(\theta_a)$ is denoted by $p(\alpha)$ where $\alpha = \theta_a$

the total brightness, or radiance, of the cavity increases as the observer approaches the source direction. Note that this results from the brightness disparity between the two facets, which increases with the angle of incidence. This effect is in contrast to Lambertian surfaces whose brightness does not vary with the viewing direction. The above illustration demonstrates that rough Lambertian surfaces are inherently non-Lambertian in reflectance. Their radiance increases as the viewer approaches the source direction. Now we present a formal treatment of the above effect.
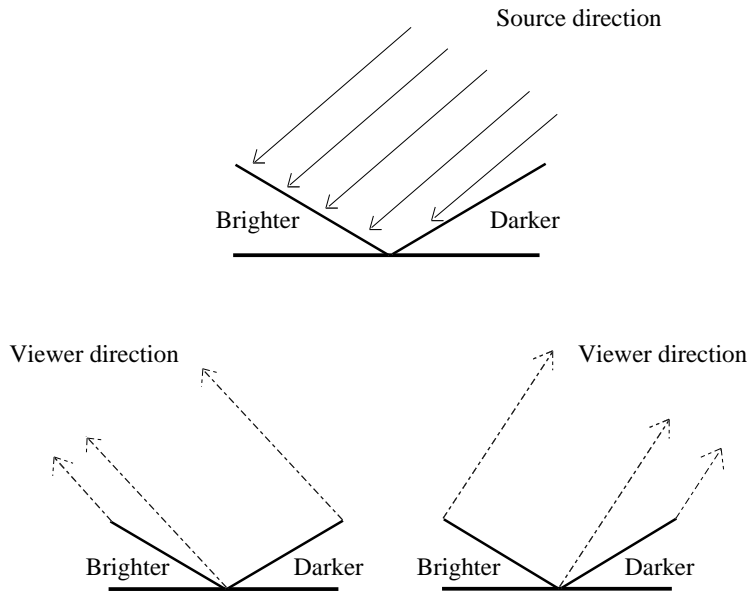

Figure 6: The radiance of the V-cavity increases as the viewer moves towards the illumination direction.

The Projected Radiance:

Consider surface area dA that is imaged by a single sensor element in the direction $\hat{v} = (\theta_r, \phi_r)$ and illuminated by a distant point light source in the direction $\hat{s} = (\theta_i, \phi_i)$. The area dA is composed of a very large number of symmetric V-cavities. Each V-cavity is composed of two facets with the same slope but facing in opposite directions. Our approach is to compute the radiance contribution of each facet on the surface. Then, the total radiance of the surface patch can be determined as an aggregate of the contributions of all facets. Consider the flux reflected by a facet with area da and normal $\hat{a} = (\theta_a, \phi_a)$. The projected area on the surface occupied by the facet is $da \cos\theta_a$ (see Figure 5). Hence, while computing the contribution of the facet to the radiance of the surface patch, we need to use the projected area $da \cos\theta_a$ and not the actual facet area da. The radiance

contribution thus determined is what we call the *projected radiance* of the facet:

$$L_{rp}(\theta_a, \phi_a) = \frac{d\Phi_r(\theta_a, \phi_a)}{(da \cos \theta_a) \cos \theta_r \, d\omega_r} \tag{7}$$

For ease of description, we have dropped the source and viewing directions from the notations for projected radiance and flux.

Total Radiance:

Now consider the slope-area distribution of facets given by $P(\theta_a, \phi_a)$. The total radiance of the surface can be obtained as the average of $L_{rp}(\theta_a, \phi_a)$ of all facets on the surface:

$$L_r(\theta_r, \phi_r; \theta_i, \phi_i) = \int_{\theta_a=0}^{\frac{\pi}{2}} \int_{\phi_a=0}^{2\pi} P(\theta_a, \phi_a) \, L_{rp}(\theta_a, \phi_a) \sin \theta_a \, d\phi_a \, d\theta_a \tag{8}$$

Thus, we have decomposed the problem of computing the radiance of any rough surface to one of computing the projected radiance for each facet on the surface. The total radiance of the surface is then obtained by integrating the product of the projected radiance and the slope-area distribution function over all facet normals.

4.1   Model for Uni-directional Single-Slope Distribution

The first surface type we consider has all facets with the same slope θ_a. Further, all V-cavities are aligned in the same direction; azimuth angles of all facets are either ϕ_a or $\phi_a + \pi$. The results obtained for this anisotropic surface will be used later in the analysis of isotropic surfaces.

Radiance from a Lambertian Facet:

Consider a Lambertian facet that is fully illuminated (no shadowing) and is completely visible (no masking) from the sensor direction. The radiance of the facet is proportional to its irradiance and is equal to $\frac{\rho}{\pi} E(\theta_a, \phi_a)$. The irradiance of the facet is $E(\theta_a, \phi_a) = E_0 < \hat{s}, \hat{a} >$, where, E_0 is the irradiance when the facet is illuminated head-on (i.e. $\hat{s} = \hat{a}$), and $<\,,\,>$ denotes the dot product between two vectors. Using the definition of radiance, the flux reflected by the facet in the sensor direction is obtained as:

$$d\Phi_r = \frac{\rho}{\pi} E_0 < \hat{s}, \hat{a} > < \hat{v}, \hat{a} > da \, d\omega_r \tag{9}$$

Substituting the above reflected flux in (7), we get:

$$L_{rp}(\theta_a, \phi_a) = \frac{\rho}{\pi} E_0 \frac{< \hat{s}, \hat{a} > < \hat{v}, \hat{a} >}{< \hat{a}, \hat{n} > < \hat{v}, \hat{n} >} = \tag{10}$$

$$\frac{\rho}{\pi} E_0 \cos \theta_i \cos \theta_a \left(1 + \tan \theta_i \tan \theta_a \cos(\phi_i - \phi_a) \right) \left(1 + \tan \theta_r \tan \theta_a \cos(\phi_r - \phi_a) \right)$$

This expression clearly indicates that the projected radiance of a tilted Lambertian facet is not equal in all viewing directions. Consequently, a rough Lambertian surface comprised of tilted facets is non-Lambertian; its radiance varies with the viewing direction. *This phenomenon is observed even in the absence of masking, shadowing, and interreflection effects.*

4.1.1 Geometric Attenuation Factor

If the surface is illuminated and viewed from the normal direction ($\hat{s} = \hat{v} = \hat{n}$), all facets are fully illuminated and visible. For larger angles of incidence and reflection, however, facets are shadowed and masked by adjacent facets (see Figure 7). In the case of *shadowing*, a facet is only partially illuminated as the adjacent facet on the V-cavity casts a shadow on it. In the case of *masking*, the facet is only partially visible to the sensor as its adjacent facet occludes it. Both these geometrical phenomena affect the projected radiance of the facet and hence must be taken into account. The result is a *geometrical attenuation factor* ($\mathcal{GAF}$) that lies between zero and unity (also see [Torrance and Sparrow-1967] [Blinn-1977]). It is the reduction in the projected radiance of a facet due to masking and shadowing effects; it equals the ratio of the facet area that is both visible and illuminated, to the total facet area.
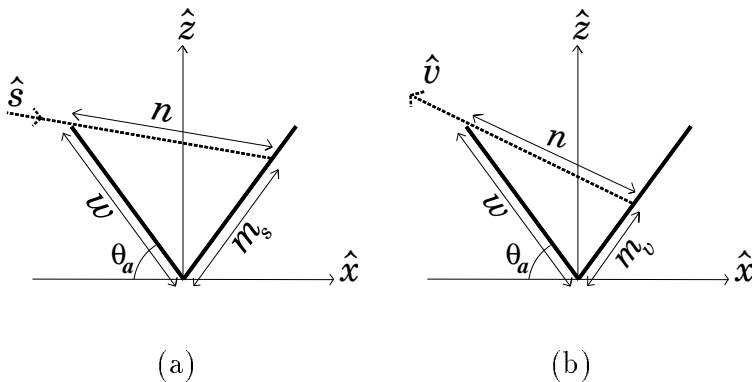

(a)   (b)

Figure 7: (a) Shadowing and (b) masking in a V-cavity.

$\mathcal{GAF}$ for Perpendicular V-Cavities:

We first restrict ourselves to V-cavities that are oriented perpendicular to the sensor-source plane. Later, the analysis is extended to arbitrary sensor and source directions. Figure 7 illustrates the masking and shadowing phenomena for the case of perpendicular V-cavities. Our objective is to determine, for a given source direction $\hat{s}$ and sensor direction $\hat{v}$ the fraction of facet area that is illuminated and visible. If the visible area is smaller than the illuminated area, masking dominates. Likewise, if the illuminated area is smaller than the visible area, shadowing dominates. We denote the length (extent on the surface plane) and width of the facet by l and w, respectively.

11

Further, m_s and m_v are sections of the facet that are shadowed and masked, respectively. The area of a facet that is both illuminated and visible is $l \cdot Min[w - m_s, w - m_v]$. The $\mathcal{GAF}$ is obtained by dividing this expression by the area $w\,l$ of the facet:

$$\mathcal{GAF} = Min\left[1 - \frac{m_s}{w}, 1 - \frac{m_v}{w}\right] \tag{11}$$

We would like to express the $\mathcal{GAF}$ in terms of the angles of incidence (source) and reflection (sensor). From the triangle $(w; m_s; n)$ in Figure 7(a), we have:

$$n \sin \theta_i = m_s \cos \theta_a + w \cos \theta_a \tag{12}$$
$$n \cos \theta_i = -m_s \sin \theta_a + w \sin \theta_a$$

By multiplying the first expression by $\cos \theta_i$ and the second by $-\sin \theta_i$ and adding the results we get:

$$\frac{m_s}{w} = -\frac{\cos(\theta_a + \theta_i)}{\cos(\theta_a - \theta_i)} \qquad \text{or} \qquad 1 - \frac{m_s}{w} = \frac{2\cos\theta_a \cos\theta_i}{\cos(\theta_a - \theta_i)} \tag{13}$$

In the above expression, the angles θ_i and θ_r are positive in the counter-clockwise direction and negative in the clockwise direction. It can be easily shown that there is no shadowing when $|\theta_a + \theta_i| \le \frac{\pi}{2}$ and $|\theta_a - \theta_i| \le \frac{\pi}{2}$, i.e. $1 - \frac{m_s}{w} \ge 1$. On the other hand, the entire facet is shadowed if $|\theta_i - \theta_a| \ge \frac{\pi}{2}$, i.e. $1 - \frac{m_s}{w} \le 0$. A similar result is obtained for masking. All these conditions are included in the following $\mathcal{GAF}$ expression for perpendicular V-cavities [6]:

$$\mathcal{GAF} = Max\left[0, Min\left[1, \frac{2\cos\theta_i \cos\theta_a}{\cos(\theta_i - \theta_a)}, \frac{2\cos\theta_r \cos\theta_a}{\cos(\theta_r - \theta_a)}\right]\right] \tag{14}$$

$\mathcal{GAF}$ for the General Case:

In the general case, source and sensor directions are arbitrary and can lie outside the plane perpendicular to the V-cavity. To make the masking/shadowing calculations tractable, we invoke the assumption that the length of facets is large compared to their width[7], i.e. $l \gg w$. Then, the analysis of masking and shadowing is reduced to the perpendicular V-cavity case by projecting the source direction $\hat{s}$ and sensor direction $\hat{v}$ onto the plane perpendicular to the cavity. These projections are done using basic trigonometry as shown in Figure 8. The projected angles are then substituted into (14),

---

[6]In the previous version of the paper, the order of the Min and Max operators was switched by mistake. The error was in the printing only and the rest of the equations and results are unchanged.

[7]When facet length is much larger than facet width, the exact shape of the cast shadow at the two ends of the facet can be ignored.

$$\sin\theta_p = \frac{\sin\theta\cos\phi}{\sqrt{\cos^2\theta + \sin^2\theta\cos^2\phi}}$$

$$\cos\theta_p = \frac{\cos\theta}{\sqrt{\cos^2\theta + \sin^2\theta\cos^2\phi}}$$
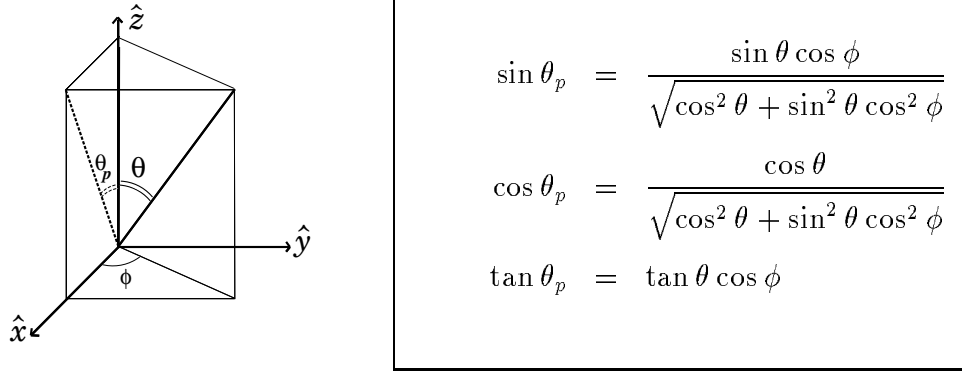
$$\tan\theta_p = \tan\theta\cos\phi$$

Figure 8: Relationship between projected and actual angles.

in place of θ_i and θ_r, to obtain the general $\mathcal{GAF}$ expression:

$$\mathcal{GAF} = Max\left[0, Min\left[1, \frac{2\cos\theta_i\cos\theta_a}{\cos\theta_i\cos\theta_a + \sin\theta_i\sin\theta_a\cos(\phi_i - \phi_a)},\right.\right.$$
$$\left.\left.\frac{2\cos\theta_r\cos\theta_a}{\cos\theta_r\cos\theta_a + \sin\theta_r\sin\theta_a\cos(\phi_r - \phi_a)}\right]\right] \qquad (15)$$

Alternatively, the $\mathcal{GAF}$ can be expressed in terms of the source, sensor, facet normal, and surface normal vectors:

$$\mathcal{GAF} = Max\left[0, Min\left[1, \frac{2<\hat{s},\hat{n}><\hat{a},\hat{n}>}{<\hat{s},\hat{a}>}, \frac{2<\hat{v},\hat{n}><\hat{a},\hat{n}>}{<\hat{v},\hat{a}>}\right]\right] \qquad (16)$$

Projected Radiance and $\mathcal{GAF}$:

The projected radiance of a Lambertian facet is obtained by simply multiplying the geometric attenuation factor with the projected radiance (10) derived under the assumption of no masking and shadowing. Table 1 details the $\mathcal{GAF}$ and the corresponding projected radiance for all cases of shadowing and masking. Note that the projected radiance is denoted as L_{rp}^1; the superscript is used to indicate that the radiance is due to direct illumination by the source. In the next section, we will use L_{rp}^2 to denote radiance due to interreflections.

4.1.2 Interreflection Factor

In our reflectance model, we also account for interreflections; light rays bouncing between adjacent facets. These effects are significant for rough surfaces with relatively high albedo values. When the surface is illuminated from large angles (θ_i) and viewed from the opposite side at large angles (θ_r), none of the facets that are visible to the sensor

13

	$\mathcal{G A F}$	$L^1_{rp}(\theta_a, \phi_a)$
No Masking or Shadowing	1	$\frac{\rho}{\pi} E_0 \frac{<\hat{s}, \hat{a}><\hat{v}, \hat{a}>}{<\hat{a}, \hat{n}><\hat{v}, \hat{n}>} =$ $\frac{\rho}{\pi} E_0 \cos\theta_i \cos\theta_a \left(1 + \tan\theta_i \tan\theta_a \cos(\phi_i - \phi_a)\right)$ $\left(1 + \tan\theta_r \tan\theta_a \cos(\phi_r - \phi_a)\right)$
Masking	$\frac{2<\hat{v}, \hat{n}><\hat{a}, \hat{n}>}{<\hat{v}, \hat{a}>}$	$\frac{\rho}{\pi} E_0 \, 2<\hat{s}, \hat{a}> =$ $\frac{\rho}{\pi} E_0 \cos\theta_i \cos\theta_a \, 2\left(1 + \tan\theta_i \tan\theta_a \cos(\phi_i - \phi_a)\right)$
Shadowing	$\frac{2<\hat{s}, \hat{n}><\hat{a}, \hat{n}>}{<\hat{s}, \hat{a}>}$	$\frac{\rho}{\pi} E_0 \frac{2<\hat{s}, \hat{n}><\hat{v}, \hat{a}>}{<\hat{v}, \hat{n}>} =$ $\frac{\rho}{\pi} E_0 \cos\theta_i \cos\theta_a \, 2\left(1 + \tan\theta_r \tan\theta_a \cos(\phi_r - \phi_a)\right)$

Table 1: Projected radiance of a facet for different masking/shadowing conditions.

are illuminated by the source. If interreflections are not considered, the radiance of the surface would be zero in this case. However, the visible facets receive light from their adjacent facets that face the source and hence are illuminated. These interreflections result in non-zero surface radiance. Our analysis and experimental results suggest that the contribution due to interreflections can be significant and cannot in general be ignored.

We have the task of modeling interreflections in the presence of masking and shadowing effects. In the case of Lambertian surfaces, the energy in an incident light ray diminishes rapidly with each interreflection bounce. Therefore, we model only two-bounce interreflections and ignore subsequent bounces. Simulations of the interreflection process were used to verify that this approximation is a good one.

In the following discussion, we refer to surface radiance due to direct illumination by the source as L^1_r and radiance due to interreflections as L^2_r. We will use the same superscripts for projected radiance. The two-bounce interreflection component for a Lambertian facet can be expressed as [Siegel and Howell-1972] [Koenderink and van Doorn-1983] [Forsyth and Zisserman-1989] [Nayar et al.-1991a]:

$$L^2_r(\vec{\mathbf{x}}) = \frac{\rho}{\pi} \int \int K(\vec{\mathbf{x}}, \vec{\mathbf{y}}) L^1_r(\vec{\mathbf{y}}) d\vec{\mathbf{y}} \tag{17}$$

where $\vec{\mathbf{x}}$ is a point on the facet whose interreflection component is determined as an integral of the radiance of all points $\vec{\mathbf{y}}$ on the adjacent facet. $K(\vec{\mathbf{x}}, \vec{\mathbf{y}})$ is the *kernel* and represents the geometrical relationship between $\vec{\mathbf{x}}$ and $\vec{\mathbf{y}}$. Since the V-cavity is long compared to its width, it can be viewed as a one-dimensional shape with translational symmetry. For such shapes, the interreflection component can be determined as an integral over the one-dimensional cross-section of the shape. The above interreflection equation is therefore reduced to:

$$L^2_r(x) = \frac{\rho}{\pi} \int K'(x, y) L^1_r(y) dy \tag{18}$$

14

where x and y are the shortest distances of points $\vec{x}$ and $\vec{y}$ from the intersection of the two facets (see Figure 9). K' is the kernel for the translational symmetry case and is derived in [Jakob-1957] and [Forsyth and Zisserman-1989] to be:

$$K'(x,y) = \frac{\pi \sin^2(2\theta_a)}{2} \frac{xy}{(x^2 + 2xy\cos(2\theta_a) + y^2)^{3/2}} \tag{19}$$

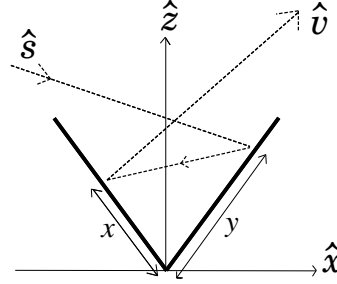We know that the normal of the considered facet is $\hat{a} = (\theta_a, \phi_a)$ and the normal of the

Figure 9: Interreflections in a V-cavity.

adjacent facet is $\hat{a}' = (\theta_a, \phi_a + \pi)$. The limits of the integral in the interreflection equation are determined by the masking and shadowing of these facets. As before, let m_v be the width of the facet which is visible to the viewer. Let m^s be the width of the *adjacent* facet that is illuminated. As in Section 4.1.1, expressions can be obtained for the visible and illuminated sections:

$$\frac{m_v}{w} = Max\left[0, Min\left[1, -\frac{<\hat{a}', \hat{v}>}{<\hat{a}, \hat{v}>}\right]\right] \tag{20}$$

$$\frac{m^s}{w} = Max\left[0, Min\left[1, -\frac{<\hat{a}, \hat{s}>}{<\hat{a}', \hat{s}>}\right]\right] \tag{21}$$

From the definition of projected radiance (7) and expression (18) we have:

$$
\begin{aligned}
L_{rp}^2 &= \frac{l<\hat{a}, \hat{v}>}{da <\hat{a}, \hat{n}> <\hat{v}, \hat{n}>} \int_{x=m_v}^{w} L_r^2(x)\, dx \\
&= (\frac{\rho}{\pi})^2 E_0 \frac{l<\hat{a}', \hat{s}><\hat{a}, \hat{v}>}{da <\hat{a}, \hat{n}> <\hat{v}, \hat{n}>} \int_{x=m_v}^{w} \int_{y=m^s}^{w} K'(x,y)dy\, dx
\end{aligned}
\tag{22}
$$

Using the following change of variables: $t = \frac{x}{w}$; $r = \frac{y}{w}$, the radiance due to two-bounce interreflections given by (22) can be written as:

$$L_{rp}^2 = (\frac{\rho}{\pi})^2 E_0 \frac{<\hat{a}', \hat{s}><\hat{a}, \hat{v}>}{<\hat{a}, \hat{n}><\hat{v}, \hat{n}>} \int_{t=\frac{m_v}{w}}^{1} \int_{r=\frac{m^s}{w}}^{1} K'(t,r)dr\, dt \tag{23}$$

Using (19), the above integral is evaluated as:

$$\int_{t=\frac{m_v}{w}}^{1} \int_{r=\frac{m^s}{w}}^{1} K'(r,t)dr\,dt = \frac{\pi}{2}\left[d(1,\frac{m_v}{w}) + d(1,\frac{m^s}{w}) - d(\frac{m^s}{w},\frac{m_v}{w}) - d(1,1)\right] \qquad (24)$$

where:

$$d(x,y) = \sqrt{x^2 + 2xy\cos(2\theta_a) + y^2} \qquad (25)$$

We refer to (24) as the *interreflection factor* ($\mathcal{IF}$). From (23), the interreflection component of the projected radiance of a facet with normal (θ_a, ϕ_a) is:

$$L_{rp}^2(\theta_a, \phi_a) = (\frac{\rho}{\pi})^2 E_0 \cos\theta_i \cos\theta_a \qquad (26)$$

$$\left(1 - \tan\theta_i \tan\theta_a \cos(\phi_i - \phi_a)\right)\left(1 + \tan\theta_r \tan\theta_a \cos(\phi_r - \phi_a)\right)\mathcal{IF}(\hat{v}, \hat{s}, \hat{a})$$

The total projected radiance of the facet is the sum of the projected radiance due to source illumination (given in Table 1) and the above interreflection component:

$$L_{rp}(\theta_a, \phi_a) = L_{rp}^1(\theta_a, \phi_a) + L_{rp}^2(\theta_a, \phi_a) \qquad (27)$$

The uni-directional single-slope surface we have considered in this section has only two types of facets with normals (θ_a, ϕ_a) and $(\theta_a, \phi_a + \pi)$. Hence, the radiance of the surface for any given source direction and sensor direction is simply the average of the projected radiances of the two facet types:

$$L_r(\theta_r, \phi_r; \theta_i, \phi_i; \theta_a, \phi_a) = \frac{L_{rp}(\theta_a, \phi_a) + L_{rp}(\theta_a, \phi_a + \pi)}{2} \qquad (28)$$

4.2   Model for Isotropic Single-Slope Distribution

We now consider a surface with V-cavities that have facets with the same slope (θ_a), but uniformly distributed in orientation (ϕ_a) in the plane of the surface. The result is a surface with isotropic roughness. The reflectance model derived for this surface is based on the results obtained in the previous section for the single-slope surface. The results obtained in this section are important as they can be used to derive a reflectance model for any isotropic surface.

From the previous section, we know the radiance $L_{rp}^1(\theta_a, \phi_a)$ of a facet with normal $\hat{a} = (\theta_a, \phi_a)$. Therefore, the radiance of the single-slope isotropic surface due to direct source illumination is determined as an integral of the projected radiance over ϕ_a:

$$L_{rp}^1(\theta_a) = \frac{1}{2\pi}\int_{\phi_a=0}^{2\pi} L_{rp}^1(\theta_a, \phi_a)d\phi_a \qquad (29)$$

Given source direction (θ_i, ϕ_i) and sensor direction (θ_r, ϕ_r), we first need to find the ranges of facet orientation ϕ_a for which the facets are masked, shadowed, masked and shadowed,

and neither masked nor shadowed[8]. The radiance for each range is given in Table 1. The problem then is to decompose the above integral into different parts, each corresponding to a different masking/shadowing range. We refer the interested reader to Appendix A.1 for details on the evaluation of integral (29). The final expression for surface radiance is found to be:

$$L^1_{rp}(\theta_a) = \frac{\rho}{\pi} E_0 \cos\theta_i \cos\theta_a \Bigg[1 + \cos(\phi_r - \phi_i)\Big(A_1(\alpha;\theta_a)\tan\beta + A_2(\beta,\phi_r - \phi_i;\theta_a)\Big) +$$

$$(1 - |\cos(\phi_r - \phi_i)|)A_3(\theta_r,\theta_i;\theta_a)\Bigg] \quad (30)$$

where, $\alpha = Max[\theta_i, \theta_r]$ and $\beta = Min[\theta_i, \theta_r]$. The expressions for the coefficients A_1, A_2, and A_3 are given in Appendix A.1. Note that the above projected radiance is the same as the total radiance of the surface $(L^1_r(\theta_r, \theta_i, \phi_r - \phi_i; \theta_a) = L^1_{rp}(\theta_a))$ since all facets on the surface have identical slope, θ_a. The derivation in Appendix A.1 does not consider multiple reflections, as the interreflection component (26) is difficult to intergrate over all cavity orientations ϕ_a. In Appendix A.2, an approximation to the interreflection component $(L^2_r(\theta_r, \theta_i, \phi_r - \phi_i; \theta_a) = L^2_{rp}(\theta_a))$ is given.

Once again, it is important to note that the radiance of the rough surface considered here is not constant with respect to the viewing direction (θ_r, ϕ_r); it is non-Lambertian. We will study this behavior more closely in the following section.

4.3   Model for Gaussian Slope-Area Distribution

The surface considered above consists of V-cavities with equal facet slope. Realistic surfaces can be modeled only if the slope-area distribution $P(\theta_a, \phi_a)$ includes a variety of different facet slopes. If the surface roughness is isotropic, the slope-area distribution can be described using a single parameter namely θ_a since the facets are uniformly distributed in ϕ_a. The radiance of any isotropic surface can therefore be determined as:

$$L_r(\theta_r, \theta_i, \phi_r - \phi_i) = \int_0^{\frac{\pi}{2}} P(\theta_a)L_{rp}(\theta_a) \sin\theta_a \, d\theta_a \quad (31)$$

where the source illumination (no interreflection) component of $L_{rp}(\theta_a)$ is given by (30). We assume the isotropic distribution to be Gaussian with mean μ and standard deviation σ, i.e. $P(\theta_a; \sigma, \mu)$. Reasonably rough surfaces can be described using a zero mean $(\mu = 0)$ Gaussian distribution:

$$P(\theta_a) = c \, e^{-\frac{\theta_a^2}{2\sigma^2}} \quad (32)$$

where the normalization constant c is:

$$1/c = \int_{\theta_a=0}^{\frac{\pi}{2}} \int_{\phi_a=0}^{2\pi} e^{-\frac{\theta_a^2}{2\sigma^2}} \sin\theta_a \, d\phi_a \, d\theta_a$$

---

[8]Imagine a V-cavity rotated about the global surface normal for any given source and sensor direction. Various masking/shadowing scenarios can be visualized.

The reflectance model is to be obtained by substituting the radiance $L_{rp}^1(\theta_a)$ given by (30) and the Gaussian distribution $P(\theta_a; \sigma, 0)$ in integral (31). The resulting integral cannot be easily evaluated. Therefore, we pursued a functional approximation to the integral that is accurate for arbitrary surface roughness and angles of incidence and reflection. In deriving this approximation, we carefully studied the functional form of $L_{rp}^1(\theta_a)$ given by (30). This enabled us to identify basis functions that can be used in the approximation. Then, we conducted a large set of numerical evaluations of the integral in (31) by varying surface roughness σ, the angles of incidence (θ_i, ϕ_i) and reflection (θ_r, ϕ_r). These simulations and the identified basis functions were used to arrive at an accurate functional approximation for surface radiance. This procedure was applied independently to the direct illumination component as well as the interreflection component.

The final approximation results are given below. Once again, let $\alpha = Max[\theta_r, \theta_i]$ and $\beta = Min[\theta_r, \theta_i]$. The direct illumination component of radiance of a surface with roughness σ is:

$$L_r^1(\theta_r, \theta_i, \phi_r - \phi_i; \sigma) = \frac{\rho}{\pi} E_0 \cos\theta_i \left[C_1(\sigma) + \right. \tag{33}$$

$$\left. \cos(\phi_r - \phi_i) C_2(\alpha; \beta; \phi_r - \phi_i; \sigma) \tan\beta + \left(1 - |\cos(\phi_r - \phi_i)|\right) C_3(\alpha; \beta; \sigma) \tan\left(\frac{\alpha + \beta}{2}\right) \right]$$

where the coefficients[9] are:

$$C_1 = 1 - 0.5\frac{\sigma^2}{\sigma^2 + 0.33}$$

$$C_2 = \begin{cases} 0.45\frac{\sigma^2}{\sigma^2 + 0.09}\sin\alpha & \text{if } \cos(\phi_r - \phi_i) \geq 0 \\ 0.45\frac{\sigma^2}{\sigma^2 + 0.09}\left(\sin\alpha - (\frac{2\beta}{\pi})^3\right) & \text{otherwise} \end{cases}$$

$$C_3 = 0.125\left(\frac{\sigma^2}{\sigma^2 + 0.09}\right)\left(\frac{4\alpha\beta}{\pi^2}\right)^2$$

Using a similar approach, an approximation to the interreflection component was also derived. In this case, the interreflection component for the single-slope isotropic surface (Appendix A.2) was used to guess the basis functions. The final approximation to the interreflection component of radiance for a surface with roughness σ is:

$$L_r^2(\theta_r, \theta_i, \phi_r - \phi_i; \sigma) = 0.17\frac{\rho^2}{\pi} E_0 \cos\theta_i \frac{\sigma^2}{\sigma^2 + 0.13}\left[1 - \cos(\phi_r - \phi_i)\left(\frac{2\beta}{\pi}\right)^2\right] \tag{34}$$

The two components are combined to obtain the total surface radiance:

$$L_r(\theta_r, \theta_i, \phi_r - \phi_i; \sigma) = L_r^1(\theta_r, \theta_i, \phi_r - \phi_i; \sigma) + L_r^2(\theta_r, \theta_i, \phi_r - \phi_i; \sigma) \tag{35}$$

---

[9]These coefficients reflect simplifications made to the ones initially presented in [Oren and Nayar-1993].

18

If the surface is extremely rough, causing the zero-mean Gaussian model to be an inaccurate approximation, an additional parameter can be used to weight the interreflection component. Our simulations show that this enables the model to stretch a bit beyond its theoretical limits. Finally, the *BRDF* of the surface is obtained from its radiance and irradiance as $f_r(\theta_r, \theta_i, \phi_r - \phi_i; \sigma) = L_r(\theta_r, \theta_i, \phi_r - \phi_i; \sigma) / E_0 \cos \theta_i$. It is important to note that the above model obeys Helmholtz's reciprocity principle (see [Beckmann and Spizzichino-1963]). *Also note that the model reduces to the Lambertian model[10] when* $\sigma = 0$.

In the next section, we present several experimental results that verify the derived diffuse reflectance model. Here, we give a brief illustration of the main characteristics of the model. Figure 10 shows the reflectance predicted by the model for a very rough surface with $\sigma = 30°$ and $\rho = 0.9$. The radiance L_r in the plane of incidence ($\phi_r = \phi_i, \phi_i + \pi$) is plotted as a function of the reflection angle θ_r for incidence angle $\theta_i = 75°$. Two curves are shown in the figure, both obtained by numerical evaluation of the integral in (31). Shortly, we shall examine the accuracy of the functional approximation.

The first curve (solid line) includes both direct illumination and interreflection components of radiance, while the second (thin line) is only the direct illumination component. Notice that these radiance plots deviate substantially from Lambertian reflectance.
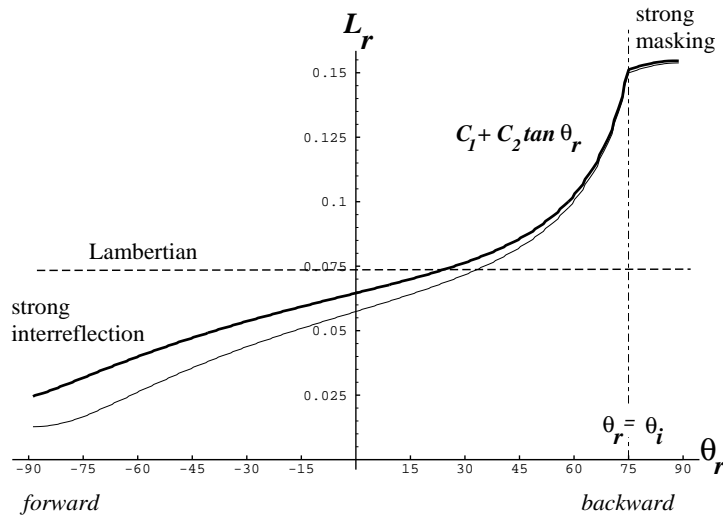

Figure 10: Diffuse reflectance in the plane of incidence for a surface with $\sigma = 30°$, $\rho = 0.90$, and incidence angle $\theta_i = 75°$. The thin line is radiance due to direct illumination (without interreflections).

Surface radiance increases as the viewing direction approaches the source direction. The curves can be divided into three sections. In the *backward* (source) direction, the radiance is maximum and gets "cut-off" due to strong masking effects when θ_r exceeds θ_i. This

---

[10]When $\sigma = 0$, $C_1 = 1$, $C_2 = 0$, and $C_3 = 0$, yielding $L_r^1 = \frac{\rho}{\pi} E_0 \cos \theta_i$.

cut-off occurs exactly at $\theta_r = \theta_i$ and is independent of roughness. In the middle section of the plot, radiance varies approximately as a scaled $tan\,\theta_r$ function with constant offset. Finally, interreflections dominate in the *forward* direction where most facets are self-shadowed and the visible facets receive light primarily from adjacent facets. This is illustrated by the difference between the two curves.

Figure 11 shows the effect of varying surface roughness. When $\sigma = 0$, the model predicts exactly Lambertian reflectance. The deviation from Lambertian behavior increases dramatically with roughness. In Figure 12(a), the effect of varying the incidence
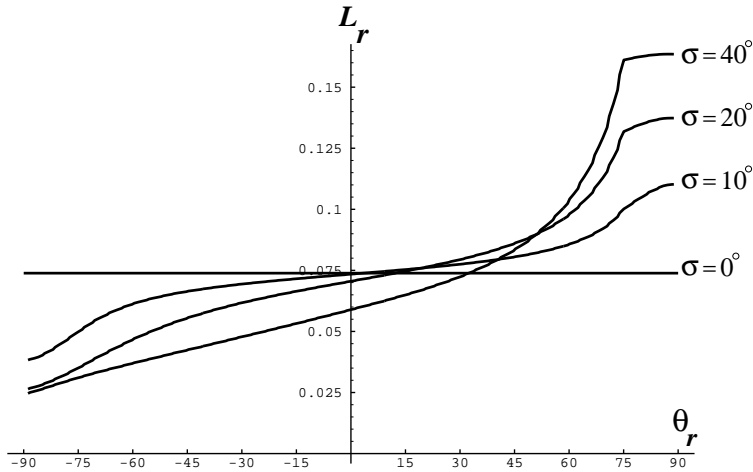

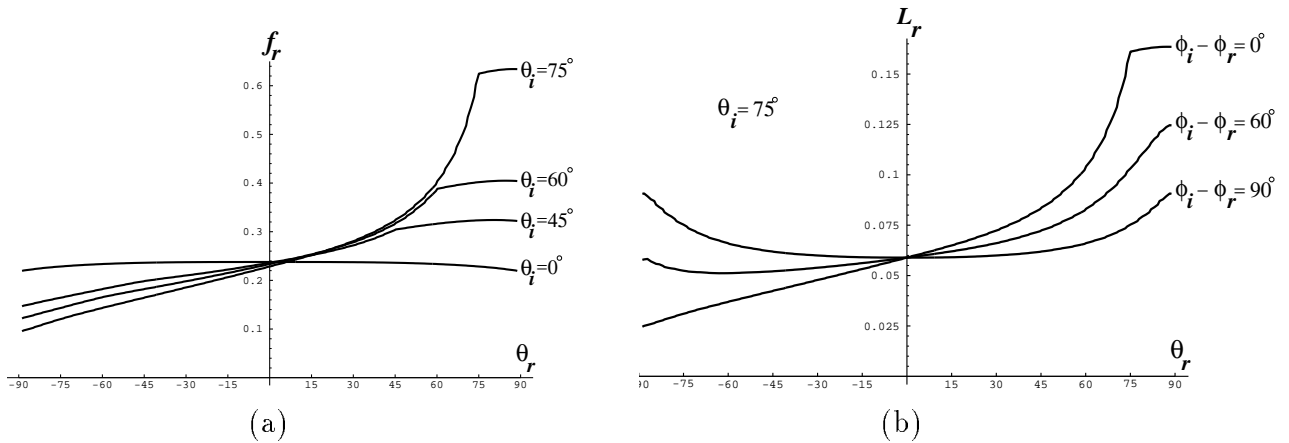Figure 11: Effect of roughness σ on surface radiance ($\theta_i = 75°$ and $\rho = 0.9$).

(a) (b)

Figure 12: (a) *BRDF* for different angles of incidence. (b) Radiance outside the plane of incidence. In both plots, $\sigma = 40°$ and $\rho = 0.9$.

angle θ_i is shown. Here we have chosen to plot *BRDF* rather than radiance to better illustrate the effect of varying θ_i. It is interesting to note that the model predicts near-Lambertian behavior for very small incidence angles ($\theta_i \approx 0$). This results from

L_r

0.25

0.2

0.15

0.1

0.05

θ_r

−90 −75 −60 −45 −30 −15   15 30 45 60 75 90

(a) $\theta_i = 0°$

L_r

0.2

0.15

0.1

0.05

θ_r

−90 −75 −60 −45 −30 −15   15 30 45 60 75 90

(b) $\theta_i = 45°$

L_r

0.2

0.15

0.1

0.05

θ_r

−90 −75 −60 −45 −30 −15   15 30 45 60 75 90

(c) $\theta_i = 60°$

L_r

0.12

0.1

0.08

0.06

0.04

0.02

θ_r

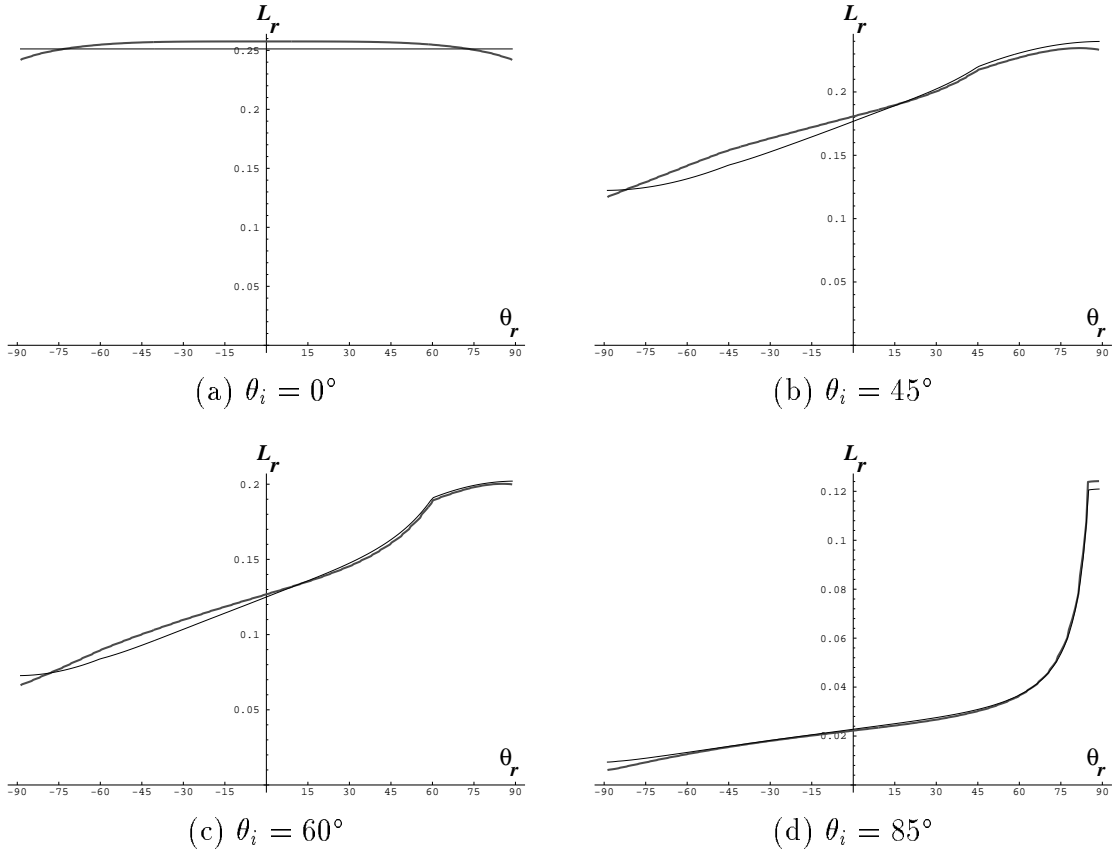−90 −75 −60 −45 −30 −15   15 30 45 60 75 90

(d) $\theta_i = 85°$

Figure 13: Comparison between numerical evaluation of the model (thick line) and functional approximation (thin line) for a surface with $\sigma = 30°$ and $\rho = 0.90$.

both facets of a V-cavity having nearly equal irradiance for small angles of incidence. As the incidence angle increases, the backscatter phenomenon begins to dominate. Figure 12(b) shows the effect of placing the sensor outside the plane of incidence. When the sensor-normal plane is perpendicular to the source-normal plane, the rough surface again exhibits near-Lambertian characteristics.

Figure 13 shows comparisons between radiance values computed by numerical evaluation of (31) (thick line) and the functional approximation (thin line) given by (33) and (34). Once again, radiance is measured in the plane of incidence ($\phi_r = \phi_i, \phi_i + \pi$). In all cases, the functional approximation proves to be very accurate.

4.4   Qualitative Model

A well-known problem in computer vision involves the use of reflectance models for computing scene properties, such as, surface orientation, reflectance, and roughness. For such problems to be tractable, it is necessary to have models with simple mathematical forms that can be inverted to estimate the parameters of interest. A major reason for the
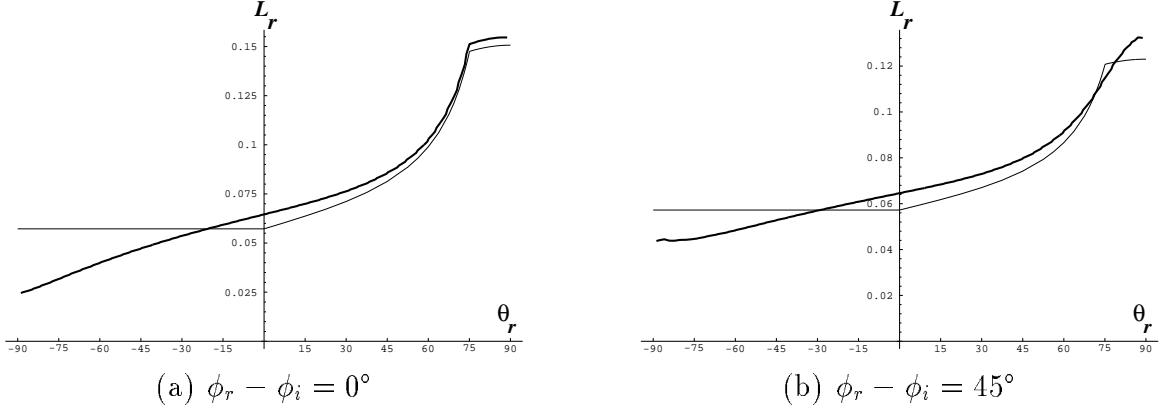
Figure 14: Comparison between numerical evaluation (thick line) and the qualitative model (thin line): (a) in the plane of incidence ($\phi_r - \phi_i = 0°$), and (b) outside the plane of incidence. In both cases, $\sigma = 30°$, $\rho = 0.90$, and $\theta_i = 75°$.

popularity of the Lambertian model is perhaps its simplicity. In this section, we propose a further simplification to the reflectance model presented in the previous section. In order to obtain this simplification, some degree of accuracy must of course be sacrificed. For the qualitative analysis of shading in images or the rendering of images for graphics and animation, a reasonably accurate model would suffice. The following simplified model was arrived at by studying, through numerous simulations, the relative significance of various terms in the functional approximation given by (33). The simulations showed that coefficient C_3 makes a relatively small contribution to the total radiance. A simpler model is thus obtained by discarding C_3 and ignoring interreflections:

$$L_r(\theta_r, \theta_i, \phi_r - \phi_i; \sigma) = \frac{\rho}{\pi} E_0 \cos \theta_i \left(A + B Max \left[0, \cos (\phi_r - \phi_i) \right] \sin \alpha \tan \beta \right) \quad (36)$$

$$A = 1.0 - 0.5 \frac{\sigma^2}{\sigma^2 + 0.33}$$

$$B = 0.45 \frac{\sigma^2}{\sigma^2 + 0.09}$$

The two coeffcients A and B are obtained directly from C_1 and C_2, respectively. Note that the qualitative model also reduces to the Lambertian model when $\sigma = 0$. In Figure 14, we have compared the qualitative model with the numerical evaluation of the model[11]. This model can be of significant practical value in applications where high accuracy is not critical.

---

[11]Discrepancies caused by the lack of the interreflection component in the qualitative model can be partially compensated by replacing the constant 0.33 in coefficient A with 0.57.

22

5   Experiments

We have conducted several experiments to verify the accuracy of the diffuse reflectance model. In the case of outdoor scenes, each sensor element (pixel) typically includes a large surface area (several inches in dimensions and often more). Commercially available reflectance measurement devices are applicable only to small samples. Consequently, we developed our own measurement device (see Figure 15). Each sample is approximatedly 2×2 inches. It is imaged using a 512×480 pixel CCD camera that is mounted at the end of a 6 foot long beam. The other end of the beam is attached to a rotary stage to facilitate precise variation of the viewing angle θ_r. The sample is illuminated using a 300 Watt incandescent light source. The solid angles subtended by the sensor and source from the sample are approximately $d\omega_i = 0.003$ steradians and $d\omega_r = 0.0009$ steradians, respectively. The illumination direction (θ_i, ϕ_i) is adjusted manually. Images of the sample are digitized and radiance is computed as the average brightness over all pixels within an image window that lies on the sample. The image window size is varied as a function of sensor direction to ensure that the same area on the sample is always used.
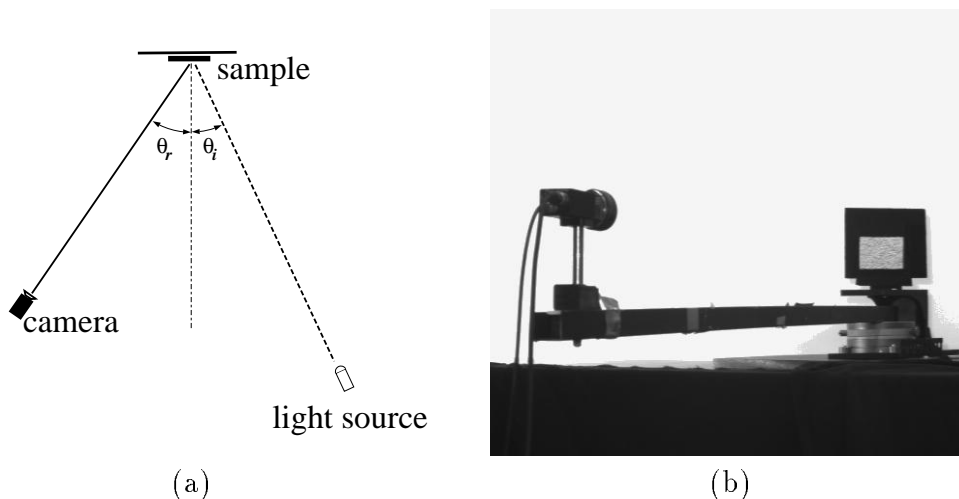

Figure 15: (a) Sketch and (b) photograph of the set-up used to measure reflectance.

Figure 16 shows results obtained for a sample of wall plaster. The sample has matte local reflectance properties but is very rough; it is exactly the type of surface that our diffuse reflectance model characterizes. Reflectance is represented by the normalized radiance $L_r(\theta_r)/L_r(0)$ where $L_r(0)$ is the radiance measured when the sample is viewed from the normal direction. The normalized radiance is also equal to the normalized $BRDF$ $f_r(\theta_r)/f_r(0)$. The radiance of each sample is plotted as a function of sensor direction θ_r for different angles of incidence θ_i. These measurements are made in the plane of incidence ($\phi_r = \phi_i = 0$). The dots represent measured radiance values while
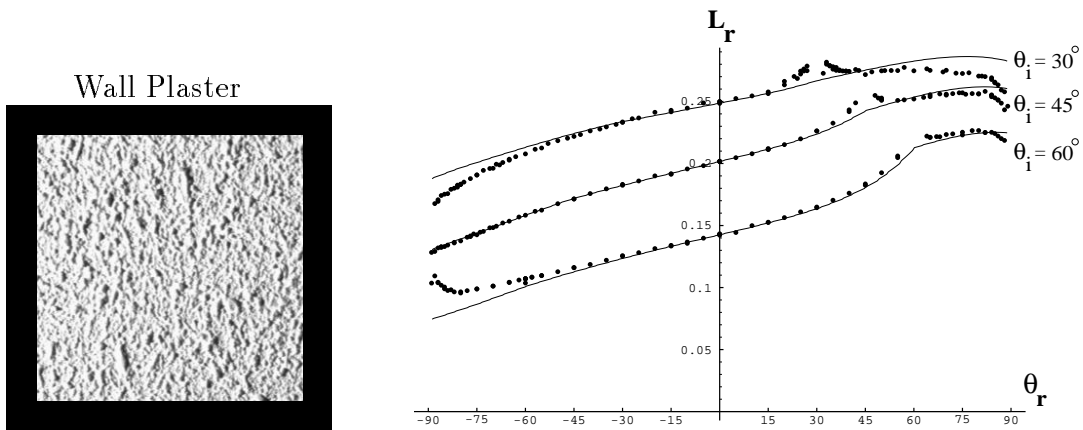
23

Wall Plaster

Figure 16: Reflectance measurement and reflectance model (using $\sigma = 30°$, $\rho = 0.90$) plots for wall plaster (sample A). Radiance is plotted as a function of sensor direction (θ_r) for different angles of incidence ($\theta_i = 30°, 45°, 60°$).

Sand Paper

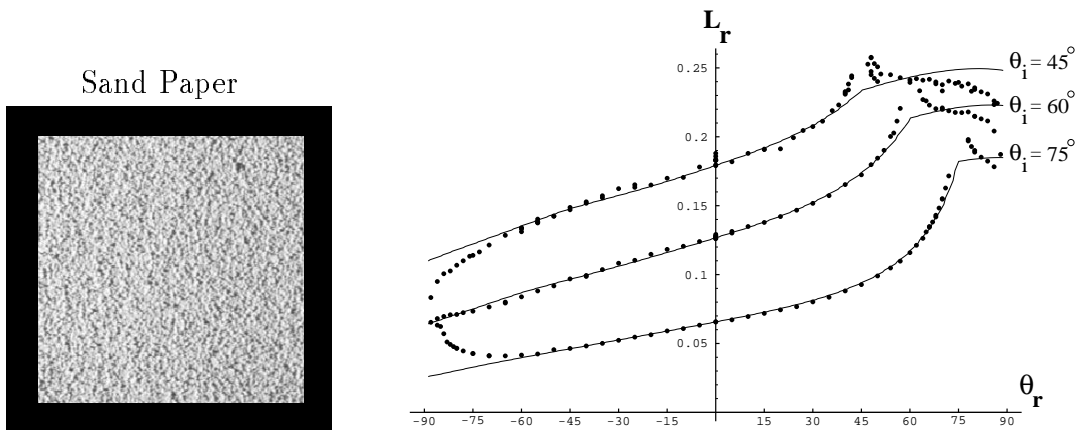Figure 17: Reflectance measurement and reflectance model (using $\sigma = 40°$, $\rho = 0.80$) plots for painted sand-paper (sample B).

Sand

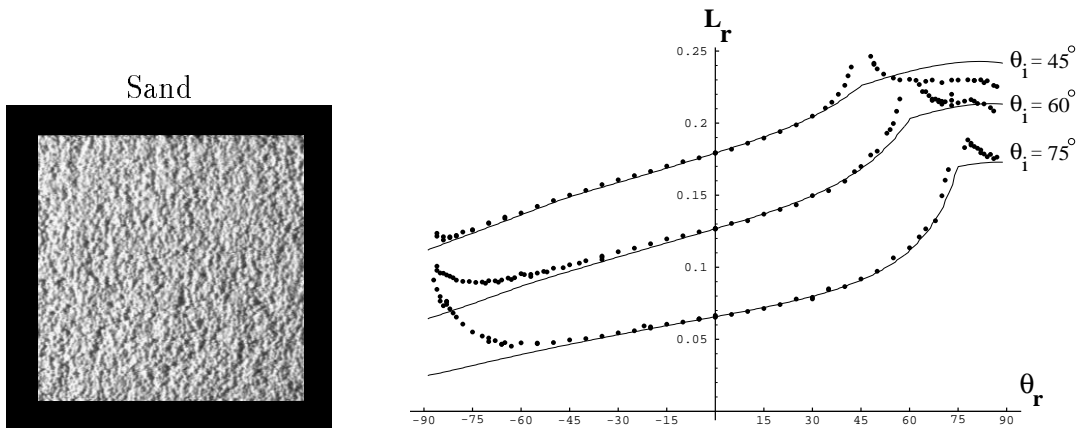Figure 18: Reflectance measurement and reflectance model (using $\sigma = 35°$, $\rho = 0.80$) plots for white sand (sample C).
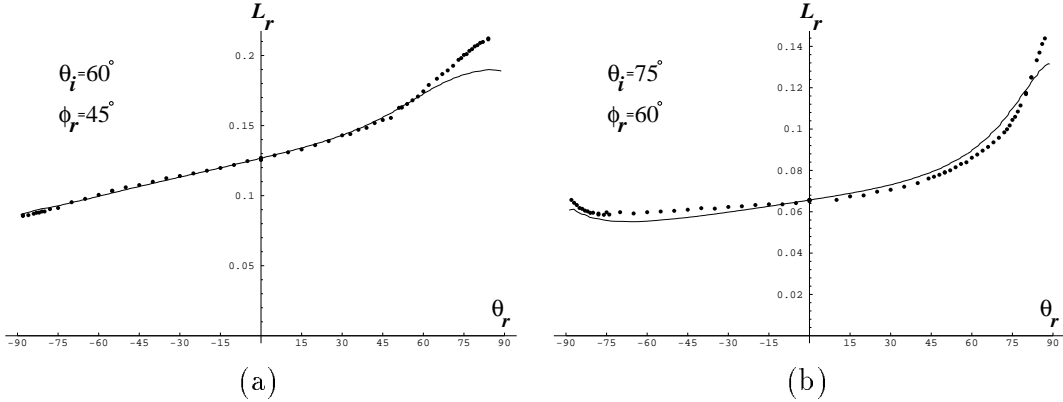
Figure 19: Reflectance measurement and reflectance model plots for sample C. These measurements were obtained for sensor directions outside the plane of incidence: (a) $\theta_i = 60°$ and $\phi_r = 45°$; and (b) $\theta_i = 75°$ and $\phi_r = 60°$.

the solid lines are predictions obtained using the reflectance model for Gaussian surface roughness. In these initial experiments, σ was selected empirically to obtain the best match between measured and predicted reflectance. Here, we have used the numerical evaluation of the model (31). This was done to demonstrate not only the accuracy of the model but also the validity of all the assumptions made while developing the model.

Similar results are presented in Figures 17 and 18 for sample B (painted sand paper) and sample C (white sand). For all three samples, radiance increases as the viewing direction θ_r approaches the source direction θ_i (backward reflection). This is in contrast to the behavior of rough specular surfaces that reflect more in the forward direction, or Lambertian surfaces where radiance does not vary with viewing direction. For all three samples, the model predictions and experimental measurements match remarkably well. In all cases, a small peak is noticed near the source direction. This phenomenon was discussed earlier in the paper and is different from the one described by our model; it is the backscatter peak studied by several researchers [Oetking-1966] [Hapke and van Horn-1963] [Hapke *et al.*-1993] [Kuga and Ishimaru-1984] [Tsang and Ishimaru-1984] and discussed in the context of machine vision in [Tagare and deFigueiredo-1991]. Discrepancies between the model and measured data found in the forward direction can be attributed partly to the long V-cavity assumption. In the case of sample C (sand), we see a small specular component in the forward direction. This is due to the specular characteristics of individual sand particles. For sample C, we have also included measurements obtained outside the plane of incidence (Figure 19). These measurements are a critical measure of the accuracy of any reflectance model but are seldom found in reflectance literature. Once again, the model and measured data are in strong agreement.

Figures 20 through 22 show results for samples that have not only a diffuse component but also a significant specular component. In these experiments, the reflectance
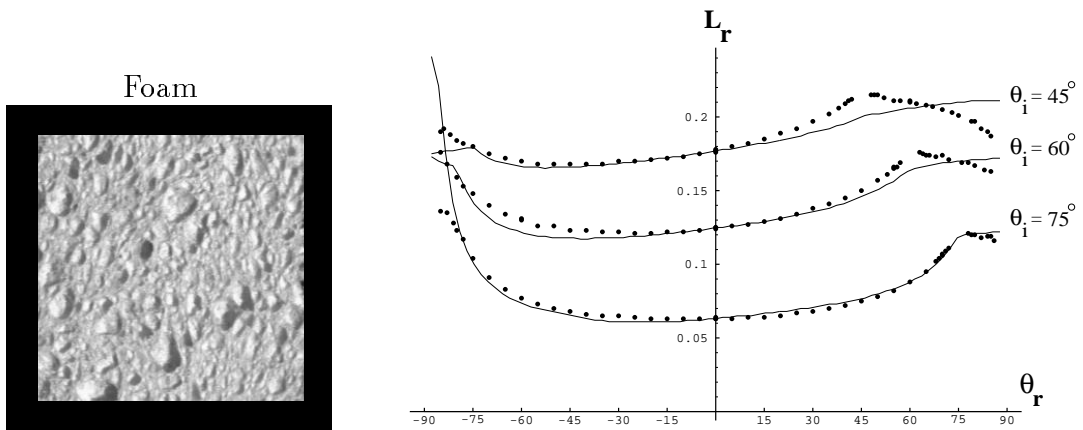
Figure 20: Reflectance measurement and reflectance model ($\sigma = 20°$, $\rho = 0.8$, $k_s/k_d = 0.019$) plots for foam (sample D).
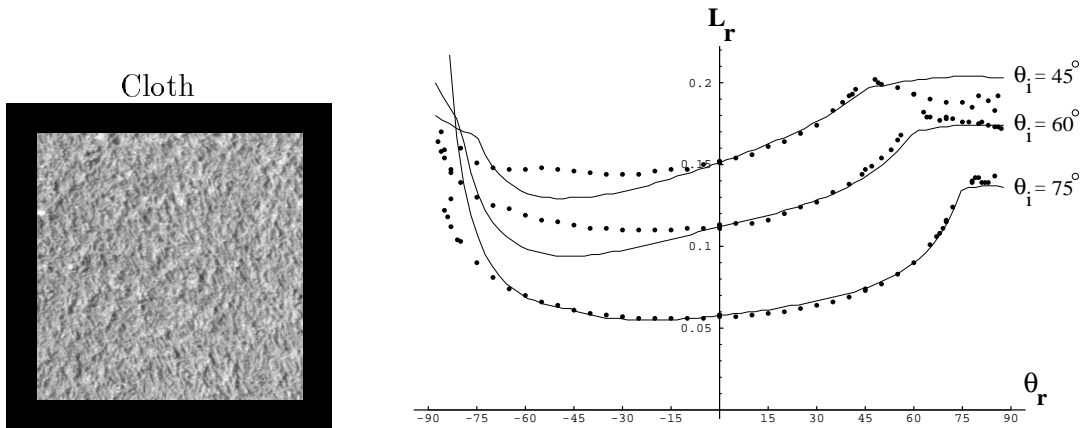

Figure 21: Reflectance measurement and reflectance model ($\sigma = 42°$, $\rho = 0.75$, $k_s/k_d = 0.085$) plots for a cotton towel (sample E).
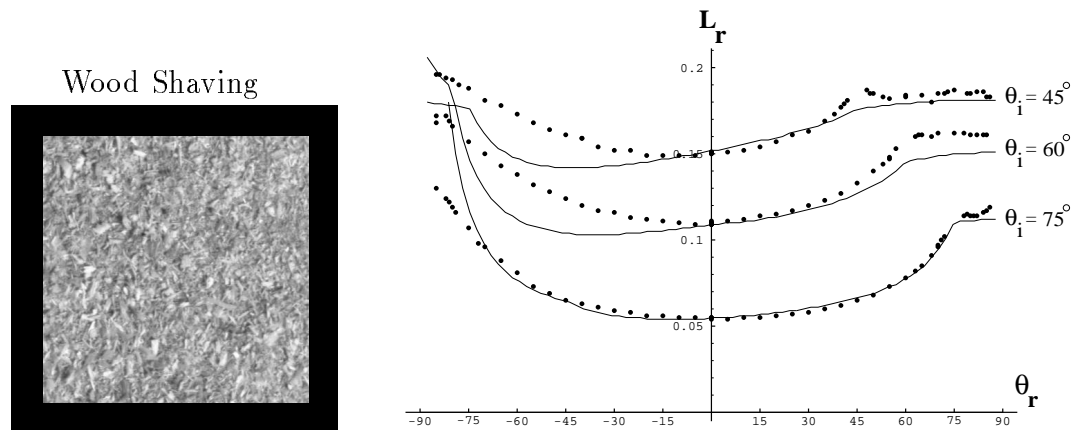

Figure 22: Reflectance measurement and reflectance model (using $\sigma = 26°$, $\rho = 0.7$, $k_s/k_d = 0.043$) plots for fine wood shavings (sample F).

model used is a linear combination of new model and the Torrance-Sparrow model [Torrance and Sparrow-1967] that describes specular, or surface, reflection from rough surfaces. We selected this model as it is based on exactly the same surface roughness assumptions (symmetric, long V-cavities) as the present model. The radiance predicted by the model is:

$$L_r^s = \frac{F(n)\mathcal{G}\mathcal{A}\mathcal{F}}{\cos\theta_r \, \cos\theta_a} \, c \, e^{-\frac{\theta_a^2}{2\sigma^2}} \tag{37}$$

where, F is the Fresnel reflection coefficient, and n is the refractive index of the surface medium. The $\cos\theta_a$ in the denominator results from using the slope-area distribution instead of the facet-number distribution (see Section 3). This model predicts a peak in the forward direction (close to the specular direction) and the distribution of the reflected radiance gets wider with increase in surface roughness σ. The total radiance is expressed as a linear combination of the diffuse and specular components:

$$L_r = k_d \, L_r^d + k_s \, L_r^s \tag{38}$$

where the diffuse component L_r^d is predicted by the model proposed in this paper. In these experiments, we used the functional approximation (33) instead of the numerical evaluation of integral (31). Moreover, the reflectance parameters σ, ρ, k_d, and k_s were estimated by fitting, using non-linear optimization, the above model to measured data. Since it is difficult to obtain meaningful estimates of n for the samples we have used, the effect of the Fresnel coefficient was ignored by assuming $F = 1$. Note that for all three samples, the diffuse model does very well in describing the increase in radiance as the viewer approaches the source, as well as the cut-off in radiance at the source direction. This despite the fact that the three samples have roughness characteristics that differ from the V-cavity model. For the foam sample, the specular component (radiance increase in the forward direction) is described well by the Torrance-Sparrow model. The Torrance-Sparrow model does only reasonably well for the cloth towel and not very well for the wood-shaving sample. The main reason for this is the following: While the Gaussian roughness model appears explicitly in the Torrance-Sparrow model, it is integrated over all facet orientations in our case. As a result, the diffuse model is less sensitive to the actual surface roughness distribution than the Torrance-Sparrow model. However, it is important to note that the combined model (38) attempts to describe very complex reflectance properties, diffuse and specular reflectance mechanisms in the presence of substantial surface roughness. Given this, the overall performance of the combined model is encouraging.

6 Implications for Machine Vision

Several algorithms in computer vision make assumptions regarding reflectance properties of objects in the scene. Incorrect modeling of reflectance naturally leads to inaccurate

results. The reflectance model presented here clearly demonstrates that rough diffuse surfaces cannot be assumed to be Lambertian in reflectance. Further, this deviation from Lambertian behavior increases with the roughness of the surface and the angle of incident light. The model can therefore be used to improve the performance of vision algorithms ranging from shape recovery to estimation of surface properties. We start by studying real and rendered images of a diffuse object. Next, we use reflectance maps to illustrate that the proposed model is, in fact, an important generalization of the Lambertian model. The model is then used to recover accurate shape information by photometric stereo. Recovered shape is compared with the shape obtained using the Lambertian model. We also discuss how diffuse reflection from non-Lambertian surfaces can affect vision algorithms for binocular stereo and motion estimation.

6.1   Real and Rendered Images

Figure 23(a) shows an image of the rough cylindrical clay vase discussed in the introduction. The image was obtained using a CCD camera. The vase is illuminated by a single light source from the sensor direction. For clarity of display, we have removed the background region from the image. Figure 23(b) shows a rendered image that is generated using the known geometry of the vase and the Lambertian model. Clearly, the real vase appears much flatter, with less brightness variation along its cross-section, than the Lambertian vase. Figure 23(c) shows an image that is rendered using the proposed reflectance model with $\sigma = 40°$ and $\rho = 0.70$. Note that the proposed model does very well in predicting the appearance of the vase. The roughness value was selected empirically. Since roughness models of actual surfaces can deviate from the V-cavity model assumed here, σ, at times, only parametrizes surface roughness and may not correspond to the actual roughness.

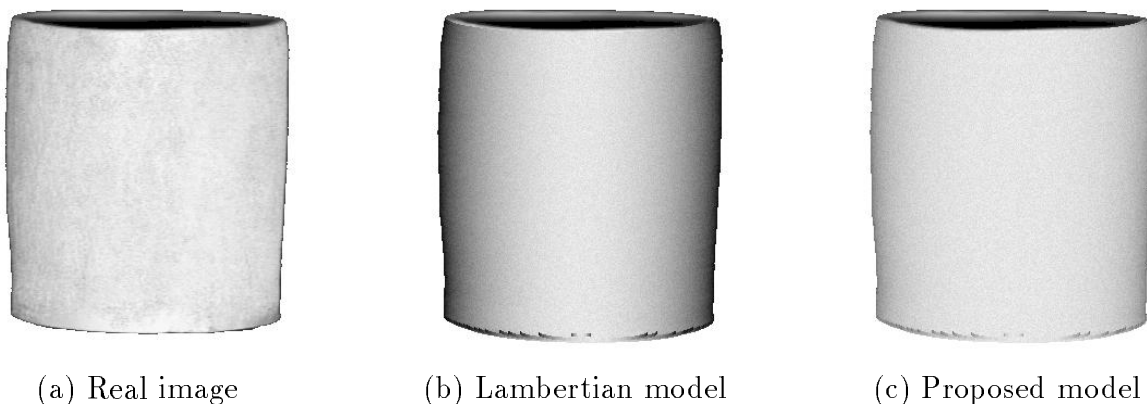(a) Real image   (b) Lambertian model   (c) Proposed model

Figure 23: Real image of a cylindrical clay vase compared with images rendered using the Lambertian and proposed models. Illumination is from the direction $\theta_i = 0°$.

Figure 24(a) compares brightness values along a cross-section of the three vase images shown in Figure 23. It is interesting to note that the brightness of the real vase
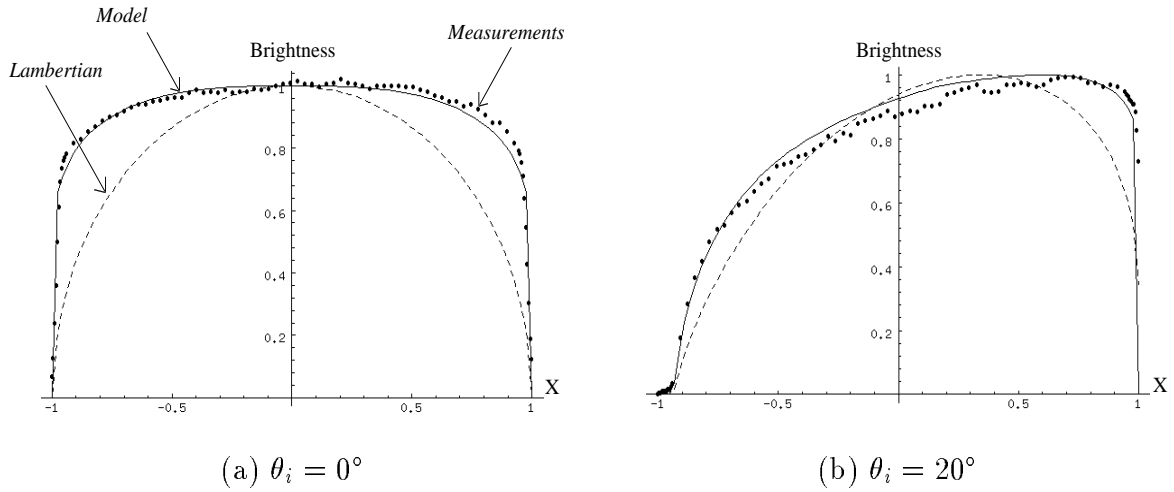
(a) $\theta_i = 0°$ (b) $\theta_i = 20°$

Figure 24: Comparison between image brightness along the cross-section of the real vase, and vases rendered using the Lambertian and proposed models.

remains nearly constant over most of the cross-section and drops quickly to zero very close to the limbs. The proposed model does very well in predicting this behavior, while the Lambertian model produces large brightness errors. Figure 24(b) shows similar plots for illumination from 20° to the right of the sensor. In this case, brightness variation on the real vase is asymmetric. Once again, the proposed model closely matches the real image. However, the Lambertian model forces the brightness close to the right limb of the vase to drop much faster than in the real image. As a result, the brightness peak predicted by the Lambertian model is way off from the actual peak.

6.2   Reflectance Maps

Reflectance maps are widely used in vision for obtaining shape information from brightness images [Horn and Brooks-1989]. For a given reflectance model and source direction, the reflectance map establishes the relationship between surface orientation, given by the gradient space parameters (p, q), and image brightness. Figure 25(a) shows the reflectance map of a Lambertian surface for illumination from the direction $(\theta_i = 10°, \phi_i = 45°)$. The same map is obtained using the proposed model with roughness $\sigma = 0$. Figure 25(b) shows the reflectance map of a rough diffuse surface with $\sigma = 60°$. Interestingly, the rough surface produces a map that appears very similar to the linear reflectance map [Horn and Brooks-1989] hypothesized for the lunar surface. The proposed reflectance model therefore establishes a continuum from pure Lambertian to lunar-like reflectance. Further, the model predicts that the linearity in the reflectance map occurs only when the viewer is close to the source.
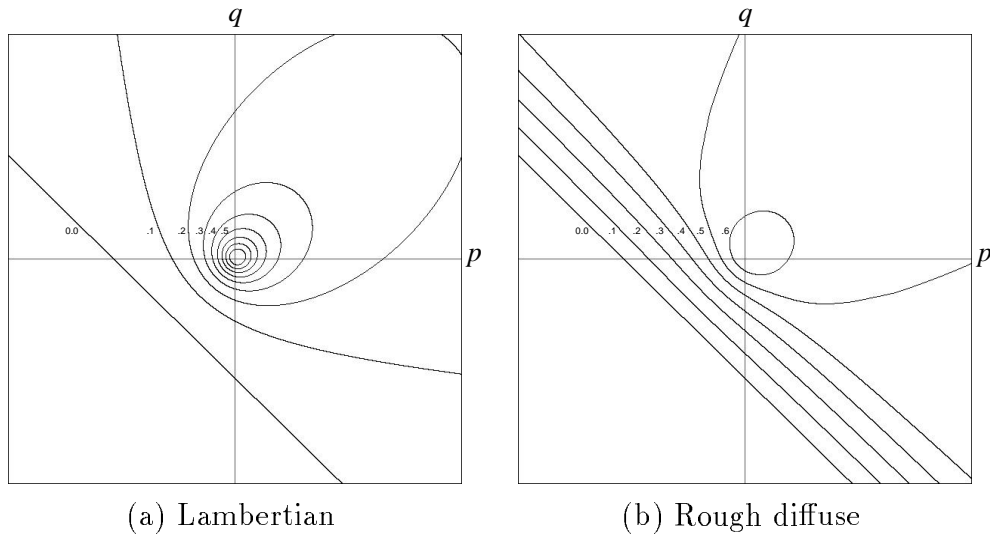
29

Figure 25: Reflectance maps for (a) Lambertian surface ($\rho = 0.9$), and (b) rough diffuse surface ($\sigma = 60°$, $\rho = 0.9$). For both maps the angles of incidence are $\theta_i = 10°$ and $\phi_i = 45°$. Note the similarity between the second map and the well-known linear reflectance map previously suggested for lunar reflectance.

6.3 Photometric Stereo

The problem of recovering shape from brightness images has been intensely researched in the past two decades. Several algorithms have been proposed, the most noteworthy of these being shape from shading [Horn and Brooks-1989] and photometric stereo [Woodham-1980]. In order to constrain the recovery problem, these techniques assume that the reflectance properties of the objects are known a-priori. For these methods to produce meaningful shape estimates, it is imperative that accurate reflectance models be used. Here, we present results obtained by applying photometric stereo to the clay vase shown in Figure 23. Photometric stereo uses multiple light sources to obtain a set of image intensities at each surface point. These intensities are used with the known source directions to compute surface orientation. Since the geometry of the vase has translational symmetry (along the cylindrical axis), only two sources are needed to compute shape. The sources were positioned at $-10°$ and $10°$ angles with respect to the sensor direction. Figure 26(a) shows the shape of the vase recovered using the Lambertian model. Figure 26(b) shows the shape computed using the proposed model and the roughness value used to render the image in Figure 23(c). Figure 27 compares height values computed along the vase cross-section using the two models. It is evident from this plot that the Lambertian model results in large errors in computed orientation and hence also in computed height. Similar errors are expected in the case of shape from shading.

In the context of visual inspection, roughness of a surface is often a measure of its quality (finish). In such cases, a radiance plot, similar to the ones shown in Figures16-

18 can be used to estimate the macroscopic roughness of the surface. Note that the source direction is known in each radiance plot. Roughness can therefore be estimated by finding the σ value for which the measured radiance data best fits the model. Due to the functional form of the model, the fitting is non-linear and an iterative technique such as the Levenberg-Marquandt [Press *et al.*-1989] method can be used. In fact, we adopted exactly this approach in fitting the combined model (38) to experimental data in Section 5.

| (a) Lambertian | (b) Model |
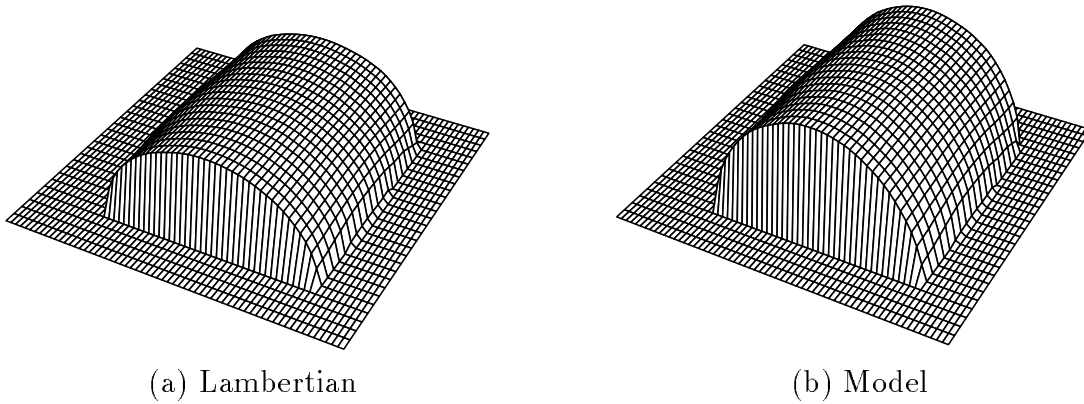
Figure 26: Shape of the vase in Figure 23(a) determined by photometric stereo using (a) the Lambertian model, and (b) the proposed model. In both cases, images were obtained using two light sources at angles $-10°, 10°$ with respect to the sensor direction.
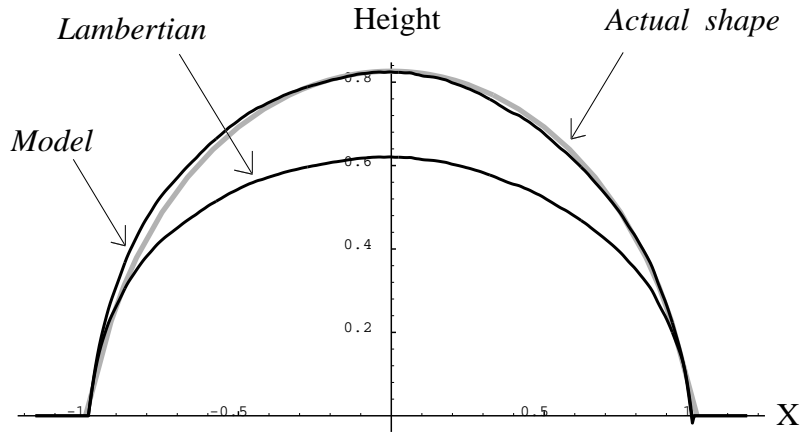

Figure 27: Actual profile of the vase compared with profiles computed using the Lambertian and proposed model ($\sigma = 40°$, $\rho = 0.70$). The Lambertian model produces large errors in computed shape.

6.4 Binocular Stereo and Motion Estimation

Binocular stereo algorithms reconstruct the shape of a scene from two or more images. The images are obtained by varying the viewing direction of the sensor. In order to compute three-dimensional coordinates of points in the scene, the correspondence between points in the different images must be established. In the case of motion estimation, objects in the scene move with respect to a stationary or moving sensor. Again, correspondence between points in consecutive images must be determined to compute optical flow estimates. There are several algorithms for matching small areas in one image with areas in other images. These algorithms assume that brightness values of points in the scene do not vary with viewing direction, i.e. a scene point has the same brightness in all images. This assumption is valid *only* if the scene is Lambertian. Our results shows that real objects can deviate substantially from Lambertian behavior; their brightness will vary with viewing direction. An interesting problem would involve developing similarity measures for correspondence that are insensitive to brightness variations due to non-Lambertian reflectance.

7 Summary

In conclusion, we have developed a comprehensive model for diffuse reflectance. A model was first derived for anisotropic surfaces that have facets with only one slope. This result was used to develop a model for isotropic surfaces with Gaussian slope-area distribution. We have also presented a qualitative model for diffuse reflection that has a simple functional form. Numerous experiments were conducted to verify the reflectance mechanism described in this paper. The results presented here have serious implications for machine vision; they show that vision algorithms based on the Lambertian assumption will not produce reliable results for a variety of real-world diffuse surfaces. We demonstrated some of these implications by using the model for rendering images of diffuse objects, studying reflectance maps of rough diffuse surfaces, and recovering shape by photometric stereo.

Acknowledgements

A Radiance of Isotropic Surface with Single-Slope Distribution

In this appendix, we outline derivations for the direct illumination and interreflection components of projected radiance for the isotropic surface discussed in Section 4.2. These results are used in Section 4.3 to derive the reflectance model for a surface with Gaussian slope-area distribution.

A.1 Radiance due to Direct Illumination

Our objective here is to evaluate the integral in (29). For any given source direction (θ_i, ϕ_i) and sensor direction (θ_r, ϕ_r), facets on the isotropic surface could be masked, shadowed, masked and shadowed, or neither masked nor shadowed. The radiance for each of these cases is given in Table 1. The problem therefore is to decompose the integral in (29) into parts, each corresponding to a different masking/shadowing range. Using basic geometry, we have identified the limits of the integrals corresponding to different ranges of shadowing/masking. These limits are represented by the *critical angles* ϕ_c^i (for shadowing) and ϕ_c^r (for masking). The critical angle ϕ_c^i is related to the slope θ_a of surface facets:

$$\phi_c^i = \begin{cases} \cos^{-1}\left(\frac{1}{\tan\theta_a \tan\theta_i}\right) & \text{if } (\tan\theta_a \tan\theta_i) > 1 \\ 0 & \text{otherwise} \end{cases} \tag{39}$$

The angle ϕ_c^r is determined using the same expression by replacing θ_i with θ_r. These critical angles are related to the masking/shadowing ranges as shown in Table 2.

Partial Shadow	No Shadow	Complete Self-Shadow
$\lvert\phi_a - \phi_i\rvert < \phi_c^i$	$\phi_c^i \leq \lvert\phi_a - \phi_i\rvert \leq \pi - \phi_c^i$	$\lvert\phi_a - (\phi_i + \pi)\rvert < \phi_c^i$
Partial Masking	No Masking	Complete Self-Masking
$\lvert\phi_a - \phi_r\rvert < \phi_c^r$	$\phi_c^r \leq \lvert\phi_a - \phi_r\rvert \leq \pi - \phi_c^r$	$\lvert\phi_a - (\phi_r + \pi)\rvert < \phi_c^r$

Table 2: Masking/shadowing and the critical angles.

Using the above critical angle expressions, Table 2, and Table 1, we decompose (29) into the sum of several integrals. Each integral can be evaluated for any fixed viewer direction. However, for arbitrary directions several cases arise and the results are not easy to use in practice. Therefore, we have chosen to express the radiance of the surface for any arbitrary viewing direction (θ_r, ϕ_r) as a weighted sum of the radiance $L_{rp\parallel}^1$ in the plane of incidence $(\phi_r = \phi_i, \phi_i + \pi)$, and the radiance $L_{rp\perp}^1$ in the perpendicular plane $(\phi_r = \phi_i \pm \frac{\pi}{2})$.

33

Radiance in the Plane of Incidence:

There are two cases to consider. In the first, $\phi_r = \phi_i$. Without loss of generality, we can assume $\phi_r = \phi_i = 0$. When $\theta_i \geq \theta_r$, radiance is obtained as:

$$
\begin{aligned}
L^1_{rp\parallel}(\theta_a) &= \tfrac{\rho}{\pi} E_0 \cos\theta_i \cos\theta_a \frac{1}{2\pi}\Big[\int_{-\phi^i_c}^{\phi^i_c} 2(1 + \tan\theta_a \tan\theta_r \cos\phi_a)d\phi_a + \\
&\quad 2\int_{\phi^i_c}^{\pi-\phi^i_c}(1 + \tan\theta_a \tan\theta_i \cos\phi_a)(1 + \tan\theta_a \tan\theta_r \cos\phi_a)d\phi_a\Big] \\
&= \tfrac{\rho}{\pi} E_0 \cos\theta_i \cos\theta_a \Big[1 + 2\tan\theta_a \tan\theta_r \frac{\sin\phi^i_c}{\pi} + \\
&\quad \frac{1}{2}\tan^2\theta_a \tan\theta_i \tan\theta_r(1 - \frac{2\phi^i_c + \sin(2\phi^i_c)}{\pi})\Big]
\end{aligned}
\tag{40}
$$

When $\theta_r \geq \theta_i$, the sensor and source directions are simply switched in the expression inside the square brackets.

In the second case, $\phi_r = \phi_i + \pi$. Again, without loss of generality, we can assume $\phi_i = 0$, $\phi_r = \pi$. When $\theta_i \geq \theta_r$, we get:

$$
\begin{aligned}
L^1_{rp\parallel}(\theta_a) &= \tfrac{\rho}{\pi} E_0 \cos\theta_i \cos\theta_a \frac{1}{2\pi}\Big[2\int_{\phi^r_c}^{\phi^i_c} 2(1 + \tan\theta_a \tan\theta_r \cos(\pi - \phi_a))d\phi_a + \\
&\quad 2\int_{\phi^i_c}^{\pi-\phi^i_c}(1 + \tan\theta_a \tan\theta_i \cos\phi_a)(1 + \tan\theta_a \tan\theta_r \cos(\pi - \phi_a))d\phi_a\Big] \\
&= \tfrac{\rho}{\pi} E_0 \cos\theta_i \cos\theta_a \Big[1 - \frac{2\phi^r_c}{\pi} + 2\tan\theta_a \tan\theta_r \frac{\sin\phi^r_c - \sin\phi^i_c}{\pi} - \\
&\quad \frac{1}{2}\tan^2\theta_a \tan\theta_i \tan\theta_r(1 - \frac{2\phi^i_c + \sin(2\phi^i_c)}{\pi})\Big]
\end{aligned}
\tag{41}
$$

Once again, when $\theta_r \geq \theta_i$, the sensor and source directions are switched in the term inside the square brackets.

Radiance in the Perpendicular Plane:

We now calculate radiance for the case where the viewer is in the plane perpendicular to the plane of incidence; i.e. $\phi_r = \phi_i \pm \frac{\pi}{2}$. Again, there are two cases to be considered. In the first case, $\phi^i_c + \phi^r_c \leq \frac{\pi}{2}$. Here, the regions of shadowing and masking do not overlap. Using these limits, the integral in (29) is evaluated as:

$$
L^1_{rp\perp}(\theta_a) = \tfrac{\rho}{\pi} E_0 \cos\theta_i \cos\theta_a
\tag{42}
$$

In the second case, we have $\phi_c^i + \phi_c^r > \frac{\pi}{2}$. Here, the regions of masking and shadowing do overlap. Without loss of generality, we can choose $\phi_i = 0$ and $\phi_r = \frac{\pi}{2}$. We define the angle γ, $0 \le \gamma \le \frac{\pi}{2}$, that separates the regions of shadowing $(-\frac{\pi}{2} + \phi_c^r \le \phi_a \le \gamma)$ and masking $(\gamma \le \phi_a \le \pi - \phi_c^i)$. γ is determined as: $\tan \theta_i \cos \gamma = \tan \theta_r \cos\left(\frac{\pi}{2} - \gamma\right)$. Then, the expression for radiance is:

$$
\begin{aligned}
L_{rp\perp}^1(\theta_a) &= \frac{\rho}{\pi} E_0 \cos\theta_i \cos\theta_a \frac{1}{2\pi}\left[\int_{-\frac{\pi}{2}+\phi_c^r}^{\gamma} 2(1 + \tan\theta_r \tan\theta_a \cos\left(\phi_a - \frac{\pi}{2}\right))d\phi_a + \right. \\
&\qquad\qquad \left. \int_{\gamma}^{\pi - \phi_c^i} 2(1 + \tan\theta_i \tan\theta_a \cos\phi_a)d\phi_a \right] \\
&= \frac{\rho}{\pi} E_0 \cos\theta_i \cos\theta_a \left[1 + \frac{1}{2} - \frac{\phi_c^i + \phi_c^r}{\pi} + \right. \\
&\qquad \left. \frac{\sqrt{\tan^2\theta_r \tan^2\theta_a - 1} + \sqrt{\tan^2\theta_i \tan^2\theta_a - 1} - \tan\theta_a \sqrt{\tan^2\theta_i + \tan^2\theta_r}}{\pi} \right] (43)
\end{aligned}
$$

Radiance in Arbitrary Azimuth Angles:

We have determined via simulations that the radiance of the isotropic surface in any arbitrary direction is well-approximated by the following weighted sum of $L_{rp\parallel}^1(\theta_a)$ and $L_{rp\perp}^1(\theta_a)$:

$$
L_{rp}(\theta_a) \approx |\cos(\phi_r - \phi_i)| L_{rp\parallel}(\theta_a) + (1 - |\cos(\phi_r - \phi_i)|)L_{rp\perp}(\theta_a) \qquad (44)
$$

This approximation was obtained by studying the expressions for the radiance components in the two planes. It is in general very accurate, with a slight over-estimation only for $\theta_r \approx \theta_i$ and $\theta_i \to \pi/2$.

Using the above linear combination of radiance in the two planes, we obtain the final expression for projected radiance. The following notation is used: $\alpha = Max[\theta_i, \theta_r]$ and $\beta = Min[\theta_i, \theta_r]$; if $\alpha = \theta_i$, $\phi_c^\alpha = \phi_c^i$, else $\phi_c^\alpha = \phi_c^r$; and the same rules apply to ϕ_c^β.

$$
L_{rp}^1(\theta_a) = \frac{\rho}{\pi} E_0 \cos\theta_i \cos\theta_a \left[1 + \cos(\phi_r - \phi_i)\Big(A_1(\alpha; \theta_a) \tan\beta + A_2(\beta, \phi_r - \phi_i; \theta_a)\Big) + \right.
$$

$$
\left. (1 - |\cos(\phi_r - \phi_i)|)A_3(\theta_r, \theta_i; \theta_a) \right] (45)
$$

where the coefficients are:

$$
A_1(\alpha; \theta_a) = \tan\theta_a \frac{2\sin\phi_c^\alpha}{\pi} + \frac{1}{2}\tan^2\theta_a \tan\alpha (1 - \frac{2\phi_c^\alpha + \sin(2\phi_c^\alpha)}{\pi})
$$

35

$$A_2(\beta, \phi_r - \phi_i; \theta_a) = \begin{cases} \frac{2\phi_c^\beta}{\pi} - \tan\theta_a \, \tan\beta \, \frac{2\sin\phi_c^\beta}{\pi} & \text{if } \cos(\phi_r - \phi_i) < 0 \\ 0 & \text{if } \cos(\phi_r - \phi_i) \geq 0 \end{cases}$$

$$A_3(\theta_r, \theta_i; \theta_a) = \begin{cases} 0 & \text{if } \phi_c^i + \phi_c^r \leq \frac{\pi}{2} \\ \frac{1}{2} - \frac{\phi_c^i + \phi_c^r}{\pi} + \\ \frac{\sqrt{\tan^2\theta_r \tan^2\theta_a - 1} + \sqrt{\tan^2\theta_i \tan^2\theta_a - 1} - \tan\theta_a\sqrt{\tan^2\theta_i + \tan^2\theta_r}}{\pi} & \text{if } \phi_c^i + \phi_c^r > \frac{\pi}{2} \end{cases}$$

A.2 Radiance due to Interreflections:

To calculate the radiance component due to interreflections, we need to evaluate the following integral:

$$L_{rp}^2(\theta_a) = \frac{1}{2\pi} \int_{\phi_a=0}^{2\pi} L_{rp}^2(\theta_a, \phi_a) d\phi_a \tag{46}$$

In Section 4.1.2, we found the interreflection factor ($\mathcal{IF}$) to be :

$$\mathcal{IF} = \frac{\pi}{2}\left[d(1, \frac{m_v}{w}) + d(1, \frac{m^s}{w}) - d(\frac{m^s}{w}, \frac{m_v}{w}) - d(1,1)\right] \tag{47}$$

The above factor cannot be easily integrated. Therefore, we use the following approximation:

$$\mathcal{IF} \approx \pi(1 - \cos\theta_a)(1 - m^s)(1 - m_v) \tag{48}$$

As in Appendix A.1, the regions of shadowing and masking were identified and the above approximation to $\mathcal{IF}$ was used to evaluate (46). The final expression for projected radiance of the isotropic surface due to interreflections is:

$$L_{rp}^2(\theta_a) \approx \frac{\rho^2}{\pi} E_0 \cos\theta_i \cos\theta_a(1 - \cos\theta_a)\Big[1 - \tag{49}$$

$$\cos(\phi_r - \phi_i)\left(\frac{2\phi_c^\beta}{\pi} + 2\tan\theta_a \tan\beta\frac{\sin\phi_c^\alpha - \sin\phi_c^\beta}{\pi} + \frac{1}{2}\tan^2\theta_a \tan\alpha \tan\beta(1 - \frac{2\phi_c^\alpha + \sin(2\phi_c^\alpha)}{\pi}))\right]$$

36

References

[Beckmann and Spizzichino, 1963] P. Beckmann and A. Spizzichino. *The Scattering of Electromagnetic Waves from Rough Surfaces.* Pergamon, New York, 1963.

[Beckmann, 1965] P. Beckmann. Shadowing of random rough surfaces. *IEEE Transactions on Antennas and Propagation*, AP-13:384–388, 1965.

[Blinn, 1977] J. F. Blinn. Models of light reflection for computer synthesized pictures. *ACM Computer Graphics (SIGGRAPH 77)*, 19(10):542–547, 1977.

[Buhl *et al.*, 1968] D. Buhl, W. J. Welch and D. G. Rea. Reradiation and thermal emission from illuminated craters on the lunar surface. *Journal of Geophysical Research*, 73(16):5281–5295, August 1968.

[Cabral *et al.*, 1987] B. Cabral, N. Max and R. Springmeyer. Bidirectional reflection functions from surface bump maps. *ACM Computer Graphics (SIGGRAPH 87)*, 21(4):273–281, 1987.

[Chandrasekhar, 1960] S. Chandrasekhar. *Radiative Transfer.* Dover Publications, 1960.

[Forsyth and Zisserman, 1989] D. Forsyth and A. Zisserman. Mutual illumination. *Proc. Conf. Computer Vision and Pattern Recognition*, pages 466–473, 1989.

[Hapke and van Horn, 1963] B. W. Hapke and Huge van Horn. Photometric studies of complex surfaces, with applications to the moon. *Journal of Geophysical Research*, 68(15):4545–4570, August 1963.

[Hapke *et al.*, 1993] B. W. Hapke, R. M. Nelson and W. D. Smythe. The opposition effect of the moon: The contribution of coherent backscatter. *Science*, 260(23):509–511, April 1993.

[Hering and Smith, 1970] R. G. Hering and T. F. Smith. Apparent radiation properties of a rough surface. *AIAA Progress in Astronautics and Aeronautics*, 23:337–361, 1970.

[Horn and Brooks, 1989] B. K. P. Horn and M. J. Brooks, editors. *Shape from Shading.* The MIT Press, 1989.

[Horn, 1986] B. K. P. Horn. *Robot Vision.* The MIT Press, 1986.

[Jakob, 1957] M. Jakob. *Heat Transfer.* Wiley, 1957.

[Kajiya, 1991] J. T. Kajiya. Anisotropic reflection model. *ACM Computer Graphics (SIGGRAPH 91)*, 25(4):175–186, 1991.

37

[Koenderink and van Doorn, 1983] J. J. Koenderink and A. J. van Doorn. Geometrical modes as a general method to treat diffuse interreflections in radiometry. *Journal of the Optical Society of America*, 73(6):843–850, 1983.

[Kuga and Ishimaru, 1984] Y. Kuga and A. Ishimaru. Retroreflectance from a dense distribution of spherical particles. *Journal of the Optical Society of America A*, 1(8):831–835, August 1984.

[Lambert, 1760] J. H. Lambert. Photometria sive de mensure de gratibus luminis, colorum umbrae. *Eberhard Klett*, 1760.

[Öpik, 1924] E. Öpik. Photometric measures of the moon and the moon the earth-shine. *Publications de L'Observatorie Astronomical de L'Universite de Tartu*, 26(1):1–68, 1924.

[Minnaert, 1941] M. Minnaert. The reciprocity principle in lunar photometry. *Astrophysical Journal*, 93:403–410, 1941.

[Nayar *et al.*, 1991a] S. K. Nayar, K. Ikeuchi and T. Kanade. Shape from interreflections. *International Journal of Computer Vision*, 6:3:173–195, 1991.

[Nayar *et al.*, 1991b] S. K. Nayar, K. Ikeuchi and T. Kanade. Surface reflection: Physical and geometrical perspectives. *IEEE Transactions on Pattern Analysis and Machine Intelligence*, 13(7):611–634, July 1991.

[Nicodemus *et al.*, 1977] F. E. Nicodemus, J. C. Richmond and J. J. Hsia. *Geometrical Considerations and Nomenclature for Reflectance*. National Bureau of Standards, October 1977. Monograph No. 160.

[Oetking, 1966] P. Oetking. Photometric studies of diffusely reflecting surfaces with application to the brightness of the moon. *Journal of Geophysical Research*, 71(10):2505–2513, May 1966.

[Oren and Nayar, 1993] M. Oren and S. K. Nayar. Diffuse reflectance from rough surfaces. *IEEE Conference on Computer Vision and Pattern Recognition*, June 1993.

[Orlova, 1956] N. S. Orlova. Photometric relief of the lunar surface. *Astron. Z*, 33(1):93–100, 1956.

[Poulin and Fournier, 1990] P. Poulin and A. Fournier. A model for anisotropic reflection. *ACM Computer Graphics (SIGGRAPH 90)*, 24(4):273–282, 1990.

[Press *et al.*, 1989] W. H. Press, B. P. Flannery, S. A. Teukolsky, and W. T. Vetterling. *Numerical Recipes in C*. Cambridge University Press, 1989.

[Siegel and Howell, 1972] R. Siegel and J. R. Howell. *Thermal Radiation Heat Transfer*. Hemisphere Publishing Corporation, third edition, 1972.

[Smith, 1967] B. G. Smith. Lunar surface roughness: Shadowing and thermal emission. *Journal of Geophysical Research*, 72(16):4059–4067, August 1967.

[Tagare and deFigueiredo, 1991] H. D. Tagare and R. J. P. deFigueiredo. A theory of photometric stereo for a class of diffuse non-Lambertian surfaces. *IEEE Transactions on Pattern Analysis and Machine Intelligence*, 13(2):133–152, February 1991.

[Torrance and Sparrow, 1967] K. Torrance and E. Sparrow. Theory for off-specular reflection from rough surfaces. *Journal of the Optical Society of America*, 57:1105–1114, September 1967.

[Tsang and Ishimaru, 1984] L. Tsang and A. Ishimaru. Backscattering enhancement of random discrete scatterers. *Journal of the Optical Society of America A*, 1(8):836–839, August 1984.

[Wagner, 1966] R. J. Wagner. Shadowing of randomly rough surfaces. *Journal of the Acoustical Society of America*, 41(1):138–147, June 1966.

[Woodham, 1980] R. J. Woodham. Photometric method for determining surface orientation from multiple images. *Optical Engineering*, 19(1):139–144, January-February 1980.